Chapter 6
A THREE-DIMENSIONAL RATE-DEPENDENT CONSTITUTIVE MODEL FOR CHALK AND SOFT ROCKS

MODEL DESCRIPTION

Rate-independent mechanical behavior of chalk is typically described by a multi-mechanism elastoplastic model which consists of a composite yield surface. The yield surface contains regions which activate the pore collapse, shear failure, and tensile failure mechanisms. Published rate-independent constitutive models for chalk are reviewed in Chapter 4.

Rate-dependent elastoviscoplastic constitutive models for chalk are similar to the rate-independent elastoplastic models but also have the capability to simulate rate-dependent behavior. As discussed in Chapters 2 and 4, elastoviscoplastic constitutive equations allow inelastic strains to occur at all stress levels. The relationship between inelastic strains components is controlled by the position of a viscoplastic potential surface. An example of a rate-dependent constitutive model with such a viscoplastic potential surface follows from the model of Gutierrez (1999) and is described in Chapter 5.

General Formulation

The proposed elastoviscoplastic constitutive model for chalk is described in the following paragraphs. The model is formulated using the properties of strain additivity, incremental elasticity, viscoplastic flow rule, and viscoplastic hardening rule as discussed in Chapter 2.

The constitutive equations are expressed in rate form. As discussed in Chapter 5, the rate-dependent model is based on the two-component assumption:

$$\dot{\varepsilon}_{ij} = \dot{\varepsilon}^{e}_{ij} + \dot{\varepsilon}^{vp}_{ij} \tag{6.1}$$

where the superscripts *e*, and *vp* indicate elastic and viscoplastic behavior, respectively. The reversible or elastic strain rate is calculated as a function of stress rate $\dot{\sigma}$:

$$\dot{\varepsilon}^{e}_{ij} = C^{e}_{ijkl}\dot{\sigma}_{kl} \tag{6.2}$$

where C^{e}_{ijkl} is the elastic compliance matrix. Equation (6.2) can be inverted as follows into a strain-rate controlled form:

$$\dot{\sigma}_{ij} = D^{e}_{ijkl}\dot{\varepsilon}^{e}_{kl} \tag{6.3}$$

where D^e_{ijkl} is the elastic constitutive matrix.

Elasticity

The matrix D^e_{ijkl} may be expressed in terms of the bulk modulus K and shear modulus G as follows:

$$D^e_{ijkl} = \left(K - \tfrac{2}{3}G\right)\delta_{ij}\delta_{kl} + G\left(\delta_{ik}\delta_{jl} + \delta_{il}\delta_{jk}\right) \tag{6.4}$$

where δ_{ij} is the Kronecker delta.

The shear modulus may be expressed in terms of the bulk modulus and Poisson's ratio ν as:

$$G = \frac{3K(1-2\nu)}{2(1+\nu)} \tag{6.5}$$

Elastic chalk behavior indicates that bulk modulus and Poisson's ratio remain approximately constant throughout loading; hence, equation (6.4) may be expressed in terms of these two elastic parameters:

$$D^e_{ijkl} = \frac{3K\nu}{(1+\nu)}\delta_{ij}\delta_{kl} + \frac{3K(1-2\nu)}{2(1+\nu)}\left(\delta_{ik}\delta_{jl} + \delta_{il}\delta_{jk}\right) \tag{6.6}$$

Inelasticity

Inelastic behavior of chalk is described by a modified form of the rate-dependent elastoviscoplastic elliptical cap model described in Chapter 5. The allowable stress states for chalk are limited by a shear failure surface and by a tension cutoff as shown in Figure 6.1.

As described in Chapter 5, the isotropic preconsolidation stress p_c is the maximum allowable mean stress in chalk for a given void ratio. The preconsolidation stress is a hardening parameter which increases as the void ratio changes, due to either the passage of time or to mechanical hardening. The preconsolidation stress is uniquely defined as a function of void ratio and of the compression coefficient λ.

In the rate-dependent time-lines model described in Chapter 5, the viscoplastic volumetric strain rate is a function of the creep parameter ψ and the volumetric age t_v. The

viscoplastic flow direction is controlled by the viscoplastic potential surface. A schematic elliptical viscoplastic potential surface is shown in Figure 6.1.

To apply the rate-dependent model to chalk in a way that accounts for its cohesive strength, the critical state line that governs the position of the viscoplastic potential surface is offset by a value equal to the attraction a as shown in Figure 6.1. This modification allows the critical state line and shear failure line to share a common origin on the p-axis, and therefore links together the pore collapse and shear failure mechanisms.

As a result of this modification, the constitutive equations presented in Chapter 5 must be modified. In all equations, the mean stress p is replaced by a transformed mean stress $\overline{p} = p + a$; the isotropic preconsolidation stress p_c is replaced by a transformed isotropic preconsolidation stress $\overline{p}_c = p_c + a$; and the equivalent hydrostatic stress p_{eq} is replaced by a transformed equivalent hydrostatic stress $\overline{p}_{eq} = p_{eq} + a$. Therefore, the viscoplastic strain rate occurs normal to the viscoplastic potential surface as described by the following equation:

$$\dot{\varepsilon}_{ij}^{vp} = \dot{\varepsilon}_{v}^{vp} \frac{\partial \varepsilon_{ij}^{vp}}{\partial \varepsilon_{v}^{vp}} = \frac{\psi}{1 + e_{eq}} \frac{1}{t_v} \frac{\partial g / \partial \sigma_{ij}}{\partial g / \partial \overline{p}} \tag{6.7}$$

where e_{eq} is the equivalent void ratio:

$$e_{eq} = \frac{1 + e}{\exp\left(\dfrac{\overline{p}_{eq} - \overline{p}}{K} \right)} - 1 \tag{6.8}$$

and the volumetric age t_v is defined as:

$$t_v = t_{v,\min} \left(\frac{\overline{p}_c}{\overline{p}_{eq}} \right)^{\frac{\lambda - \kappa}{\psi}} \tag{6.9}$$

where κ is the recompression coefficient and $t_{v,\min}$ is the minimum possible volumetric age. The viscoplastic potential surface is described by the following equation:

$$g = q^2 - G_\theta^2 M^2 R^2 \overline{p}_{eq}^2 + G_\theta^2 M_2^2 \left(\overline{p} - R\overline{p}_{eq} \right)^2 \tag{6.10}$$

where G_θ is the William-Warnke (1975) third-invariant scaling factor, which is a function of the Lode angle θ. The transformed equivalent hydrostatic stress $\overline{p}_{eq}$ is defined as:

$$\bar{p}_{eq} = \frac{G_\theta M_2^2 \bar{p} - \sqrt{G_\theta^2 M^2 M_2^2 \bar{p}^2 + q^2 \left(M^2 - M_2^2\right)}}{G_\theta R\left(M_2^2 - M^2\right)} \tag{6.11}$$

where M, R, and M_2 have the same meanings as defined in Chapter 5. The meanings of these parameters with respect to the constitutive model are shown in Figure 6.1(a).

The ultimate frictional strength of chalk is described by a Mohr-Coulomb-type shear failure surface which appears as a line in p-q space. Chalk has cohesion; hence the shear failure surface intersects the q-axis at some positive value, and also intersects the p-axis at some negative value as shown in Figure 6.1(b). The shear strength envelope has a slope equal to the adjusted failure shear stress ratio of $\bar{\eta}_f$ in p-q space, and intersects the p-axis at a value of ($-a$) where a is the attraction discussed previously. The shear strength is also scaled by the third-invariant William-Warnke scaling parameter G_θ. The yield function for the shear failure surface is:

$$f = q - G_\theta \bar{\eta}_f \left(p + a\right) = q - G_\theta \bar{\eta}_f \bar{p} \tag{6.12}$$

The shear failure surface is assumed to be nonhardening and time-independent, so neither the adjusted failure shear stress ratio $\bar{\eta}_f$ nor the attraction a changes due to mechanical loading or passage of time.

The shear strength envelope overestimates the strength of chalk in tension as measured in Brazilian tests. Therefore, a tensile failure surface is included in the chalk constitutive model. The tensile failure surface appears as a vertical line with intercept ($-p_t$) in p-q space, where p_t is the tensile strength. The yield function for the tensile failure surface is:

$$f = p + p_t = \bar{p} - a + p_t \tag{6.13}$$

The tensile failure surface is assumed to be nonhardening and time-independent, so the tensile strength p_t does not change due to mechanical loading or passage of time

The ultimate or failure shear surface appears is dependent on the relative value of the intermediate principal stress. The shear failure surface appears as the William-Warnke smooth approximation to the irregular hexagon of the Mohr-Coulomb surface, in the π-plane. This shape of the shear failure surface in the π-plane is also adopted for the elliptical cap yield surface. The third-invariant dependence using the William-Warnke surface appears as the function G_θ, which

scales the aspect ratio of the elliptical viscoplastic potential surface in the π-plane. The function G_θ is a function of the Lode angle θ and the scaling parameter k:

$$G_\theta = \frac{c_1 \cos\left(\theta - \frac{\pi}{6}\right) + \sqrt{c_2\left(c_3 + c_4\right)}}{c_2 + c_4} \tag{6.14}$$

$$\begin{aligned} \text{where} \quad c_1 &= 2\left(1 - k^2\right) \\ c_2 &= \left(2k - 1\right)^2 \\ c_3 &= k\left(5k - 4\right) \\ c_4 &= 2c_1 \cos^2\left(\theta - \frac{\pi}{6}\right) \end{aligned}$$

where k is the ratio of the strength in triaxial extension to the strength in triaxial compression. For triaxial compression conditions, G_θ equals its maximum value of 1, while for triaxial extension conditions, G_θ equals its minimum value of k. For other intermediate principal stress conditions, G_θ lies somewhere between these extremes; see Figure 6.1(b).

The way the viscoplastic potential and the shear failure surface are defined, the direction of viscoplastic flow is constant at any point along the shear failure surface. Viscoplastic flow is then non-associated on the shear failure surface. Therefore, the plastic flow direction is defined and continuous at all legal points in stress space. If $\bar{\eta}_f < M$, the maximum allowable adjusted shear stress ratio is less than that at critical state and plastic flow during shear failure is contractant; if $\bar{\eta}_f = M$, the maximum allowable adjusted shear stress ratio is equal to that at critical state and plastic flow during shear failure is at constant volume; and if $\bar{\eta}_f > M$, the maximum allowable adjusted shear stress ratio is greater than that at critical state and plastic flow during shear failure is dilatant.

Required Parameters

For the rate-dependent constitutive model, 12 parameters are required to fully describe material behavior. These parameters are listed in Table 6.1. As indicated, 2 parameters describe elastic behavior, 7 parameters describe rate-dependent pore collapse behavior, 1 parameter describes the shear failure surface, 1 parameter describes the tensile failure surface, and 1 parameter describes third-invariant effects. Procedures to obtain values for these parameters are described in the next

subsection. Correlations for several of these parameters and the expected range of values for North Sea chalks are given in the following section.

Determination of Parameters

Values for the required parameters may be determined from the results of laboratory tests. Procedures to determine appropriate parameter values, and example figures showing the procedures at work for North Sea chalks, are described in the following paragraphs.

The bulk modulus K is the slope of the initial, elastic portion of the mean stress-volumetric strain curve for a hydrostatic compression test (Figure 6.2a).

The Poisson's ratio ν may be calculated from the slope of the initial, elastic portion of the p-q stress path for a K_0 compression test (Figure 6.2b). The slope x is equal to $\Delta q / \Delta p$, which under K_0 conditions may be simplified to:

$$x = \frac{3(1-2\nu)}{1+\nu} \tag{6.15}$$

Equation (6.15) may then be solved for ν:

$$\nu = \frac{3-x}{6+x} \tag{6.16}$$

The compression coefficient λ is equal to the slope of the elastoplastic portion of the stress-strain curve, shown in e-ln p space, from a constant-rate hydrostatic compression test (Figure 6.3). The reference time-line anchor N may also be found from this curve by extrapolating the slope λ to the value $p = 1$, as shown in Figure 6.3. For hydrostatic compression tests performed over a large strain range, it is also possible to determine by curve matching the parameter A to fit a nonlinear e-ln p envelope of the type described in Chapter 5. However, for simplicity the parameter A is usually taken to be zero.

If the values for void ratio e, isotropic preconsolidation stress p_c, and compression coefficient λ are known, the value of N may be calculated using a rearranged form of equation (5.7):

$$N = e + \lambda \ln(p_c) \tag{6.17}$$

The creep parameter ψ and the minimum volumetric age $t_{v,\min}$ are the slope and intercept of the tangent to the linear portion of the creep time-strain curve shown in Δe-ln t space for a σ-constant creep test under K_0 compression conditions (Figure 6.4).

The adjusted failure shear stress ratio $\overline{\eta}_f$ and the attraction a are the slope and intercept of the best-fit straight line that passes through the shear failure points in p-q space for a set of drained and/or undrained triaxial compression tests (Figure 6.5).

The tensile strength p_t is determined and reported directly from Brazilian (*i.e.*, splitting tension) tests. Goodman (1989) provides details regarding stress distribution under Brazilian test conditions.

The William-Warnke scaling parameter k is the ratio of the slopes of the best-fit straight lines through shear failure points from triaxial extension and triaxial compression tests (Figure 6.6).

The critical state slope M and eccentricity parameter R are found by minimizing residuals between observed yield points and a best-fit parabola (Figure 6.7a) as follows. This procedure requires data from a set of drained triaxial compression tests on overconsolidated samples with the same isotropic preconsolidation stress p_c. For each sample, the yield stress may be found by identifying the change in slope on the stress-strain curves (Figure 6.7b). Then for each yield point, the adjusted shear stress ratio $\overline{\eta}(=q/\overline{p})$ and the ratio $\overline{p}_c/\overline{p}$ are calculated. A predicted value of $\overline{p}_c/\overline{p}$ may be found using a rearranged form of equation (6.11) for the observed values of $\overline{\eta}$:

$$\frac{\overline{p}_c}{\overline{p}} = \frac{MR^2 + (R-1)\sqrt{M^2R^2 + \overline{\eta}^2(1-2R)}}{MR(2R-1)} \tag{6.18}$$

The best-fit values of M and R may be found by minimizing the sum of the absolute value residuals between the observed and predicted values of $\overline{p}_c/\overline{p}$ by optimizing the values of M and R. This minimization procedure can be performed using the Solver function of Microsoft Excel, or a similar multivariable optimization function.

CORRELATIONS AND RANGE OF VALUES FOR NORTH SEA CHALKS

Many laboratory tests must be performed to determine value for all parameters as described in the previous section. Moreover, the mechanical properties of chalk may vary substantially in

space due to variations in lithology, porosity, and other factors. The many laboratory tests that have been performed over the years on North Sea chalks provide a good database to predict the properties of these chalks. It has been observed in these historical tests that several of the required parameters appear to vary predictably as a function of porosity, or to vary within a relatively small range of values. The purpose of this section is to show these correlations and/or observed range of values for the North Sea chalks. This way, a reasonable set of values may be selected for numerical analyses in lieu of performing all the laboratory tests required.

As explained in Chapter 3, the elastic behavior of chalk is best described by a linear elastic model in which bulk modulus is dependent on porosity. The data showing the relationship between bulk modulus and porosity for all chalks is repeated from Chapter 3 and shown in Figure 6.8. The best-fit relationship for all oil- and gas-saturated chalks is:

$$K(\text{in MPa}) = 86000\exp(-9.4n) \tag{6.19}$$

where n is porosity (dimensionless). A better fit may be obtained using samples only from an individual chalk field.

For oil-saturated chalk, the range of observed values for Poisson's ratio ν is from 0.20 to 0.27, with a mean value of 0.24, a median value of 0.24, and a standard deviation of 0.026. The values of Poisson's ratio show no correlation with porosity, as shown in Figure 6.9.

The observed values for compression coefficient λ for oil-saturated chalks range from 0.086 to 0.22 and tend to increase for more porous chalks, as stated in Chapter 3. The initial isotropic preconsolidation stress and compression coefficient observed in chalk both vary consistently as a function of porosity. The data for all chalks showing the relationships between isotropic preconsolidation stress p_c and porosity n, and between compression coefficient λ and porosity n, are repeated from Chapter 3 in Figure 6.10. The best-fit relationships for all oil-saturated chalks are:

$$p_c(\text{in MPa}) = 360\exp(-7.0n) \tag{6.20}$$

$$\lambda = 0.024\exp(4.5n) \tag{6.21}$$

By substituting the correlations in equations (6.20)-(6.21) into equation (6.17), a correlation between the reference time-line anchor N and porosity n for oil-saturated chalks is obtained:

$$N = \frac{n}{1-n} + (0.141 - 0.168n)\exp(4.5n) \tag{6.22}$$

As for any parameter correlated across chalks from all of the North Sea chalks, a better fit may be obtained by using only data from a single chalk field.

The attraction *a* for outcrop chalks is approximately zero; see Figure 3.24 for data from Butser-Hill and Stevns Klint outcrops. For all oil-saturated chalks, the average value for attraction is approximately 4 MPa, as shown in Figure 6.11a, although the apparent attraction (or cohesion) decreases when only deep-sea chalks are plotted (Figure 6.11b).

The adjusted failure shear stress ratio $\overline{\eta}_f$ varies consistently with porosity as described in Chapter 3. The data showing the relationship between failure shear stress ratio and porosity for all chalks is shown in Chapter 3 and duplicated in Figure 6.12. Assuming $a = 4$ MPa for deep-sea chalks and $a = 0$ for outcrop chalks, the best-fit relationship for triaxial compression and unconfined compression test data for all oil- and gas-saturated chalks (Figure 6.12a) is:

$$\overline{\eta}_f = 5.4\exp(-3.9n) \tag{6.23}$$

Although a slightly better fit is obtained using only triaxial compression test data for deep-sea chalks (Figure 6.12b):

$$\overline{\eta}_f = 5.5\exp(-4.0n) \tag{6.24}$$

As for the other model parameters, a better fit may be obtained using samples only from an individual chalk field.

The critical state slope *M* and eccentricity parameter *R* both appear to vary as a function of porosity. Chalks are almost always slightly contractant during shear; therefore, $M > \overline{\eta}_f$. As described in Chapter 3 and shown in Figure 6.13, the adjusted shear stress ratio under K_0 conditions varies with porosity:

$$\overline{\eta}_{K_0} = 0.60\ln(n) + 1.17 \tag{6.25}$$

An expression for *R* may be found by substituting equation (5.60) into equation (5.58), and setting the resulting expression equal to zero:

$$\frac{\overline{\eta}_{K_0} M^2 \left[\left(\frac{R}{1-R} \right)^2 - 1 \right]}{M^2 \left(\frac{R}{1-R} \right)^2 \left(\sqrt{M^4 \left(\frac{R}{1-R} \right)^2 + \overline{\eta}_{K_0}^2 M^2 \left[1 - \left(\frac{R}{1-R} \right)^2 \right]} - M^2 \right)} = \frac{2}{3} \tag{6.26}$$

Assuming that $M = 1.01\,\overline{\eta}_f$, the best-fit equations for shear stress ratio $\overline{\eta}_{K_0}$ and critical state slope M as a function of porosity may be substituted into a simplified version of equation (6.26):

$$3.91R^2 \exp(-4.1n)\left[\sqrt{[5.87\exp(-4.1n)]^2 R^2 + (0.015n + 0.011)^2 (1-2R)} + [5.87\exp(-4.1n)](R-1) \right] + (0.015n + 0.011)(2R-1)(R-1) = 0 \tag{6.27}$$

The value for R for a given porosity n is then found by numerically solving equation (6.27). The resulting variation in R with n may then be described by the following equation:

$$R = 2.5n^2 + 0.26n + 0.103 \tag{6.28}$$

The tensile strength p_t varies consistently with porosity as described in Chapter 3. The data showing the relationship between tensile strength and porosity for all chalks, as shown in Chapter 3, is shown again in Figure 6.14. The best-fit relationship for all oil- and gas-saturated chalks is:

$$p_t = 0.061 n^{-2.82} \tag{6.29}$$

As for the other model parameters, a better fit may be obtained using samples only from an individual chalk field.

The William-Warnke parameter k has a value of 0.71 for the data from outcrop chalks shown in Figure 3.32, and a value of 0.57 for Lixhe chalk data shown in Figure 6.6. A similar value ($k \approx 0.6$) fits the data for several chalks shown in Figure 3.34.

Only a sparse amount of experimental data exists to estimate values for k. It is possible to estimate the variability in k with porosity as follows: The three-dimensional Mohr-Coulomb criterion as described in Chapter 3 may be combined with the correlation to adjusted failure shear stress ratio $\overline{\eta}_f$ in equation (6.23) to yield the following correlation between k and porosity:

$$k = \frac{1}{1 + 0.98\exp(-4.1n)} \tag{6.30}$$

For oil-saturated chalk, the range of observed values for creep parameter ψ is from 0.0014 to 0.0054, with a mean value of 0.0034 and a median value of 0.0033. The range of observed values for minimum volumetric age $t_{v,\min}$ is from 0.1 to 3 hours, with a mean value of 0.7 hours and a median value of 0.7 hours. The values of creep parameter ψ and minimum volumetric age $t_{v,\min}$ both show no correlation with water saturation (when primarily oil-saturated) or porosity, as shown in Figure 6.15. However, a positive correlation appears to exist between the creep parameter and minimum volumetric age, as shown in Figure 6.16. As for lab tests available to determine third-invariant parameter values, only a small number of σ-constant creep tests have been performed to determine best-fit values for rate-dependent parameters.

Pore fluid composition strongly influences time-dependent behavior. A description of the effects of pore fluid composition on chalk mechanical behavior and the chalk model is included in Chapter 8.

COMPARISON WITH EXPERIMENTAL RESULTS

Many constitutive tests have been performed in the laboratory, under various stress- and strain-controlled conditions, to determine the constitutive behavior of North Sea chalk. The rate-dependent chalk model was used to simulate several of these results for oil-saturated deep-sea chalks as described in this section. For all simulations (except those simulating chalks from the Dan field, as described below), the correlations with porosity described in the previous section were used to determine values for bulk modulus K, preconsolidation stress p_c, compression coefficient λ, adjusted failure shear stress ratio $\overline{\eta}_f$, and tensile strength p_t. Initial void ratio for each sample is known, so equation (6.17) may be used to determine the value for the reference time-line anchor N. It is assumed that $M = 1.01\,\overline{\eta}_f$. Equation (6.28) is then used to find an appropriate value for the eccentricity parameter R. For all deep-sea chalks, attraction a is assumed to equal 4MPa. Poisson's ratio ν is assumed to equal 0.24 for all chalks. The creep parameter ψ and minimum volumetric age $t_{v,\min}$ are assumed to equal 0.0034 and 1 hour, respectively, for all oil-saturated chalks. All tests simulated here were performed under triaxial compression conditions (θ = -30º), so the value of the William-Warnke scaling parameter k does not influence the results.

The simulations shown here include 6 tests from the Ekofisk A field, 9 tests from the Valhall field (including both the Hod 1 and Tor zones), and 6 tests from the Dan field. Simulated loading conditions include hydrostatic compression, K_0 compression, undrained triaxial compression, drained triaxial compression, and special stress paths 5 and 6, which include multiple loading conditions. Values for all required model parameters are shown in Table 6.2 for the Ekofisk A field simulations, in Table 6.3 for the Valhall field simulations, and in Table 6.4 for the Dan field simulations.

Comparisons between the lab results and simulation results for the tests on samples from the Ekofisk A field are shown in Figures 6.17 through 6.22. The simulations include hydrostatic compression (Figure 6.17), K_0 compression (Figure 6.18), drained triaxial compression (Figure 6.19), undrained triaxial compression (Figures 6.20 and 6.21), and stress path 5 (Figure 6.22). From these results, it may be concluded that the model is able to reproduce the mechanical behavior of oil-saturated chalk reasonably well. Some of the values for the model parameters obtained from the correlations may be seen to contain significant error. The most noticeable errors for this suite of tests are in the bulk modulus for File 341, and in the preconsolidation stress for Files 330 and 341.

Comparisons between the lab results and simulation results for the tests on Valhall field samples are shown in Figures 6.23 through 6.31. The simulations include hydrostatic compression (Figures 6.23 and 6.24), K_0 compression (Figures 6.25 and 6.26), drained triaxial compression (Figure 6.27), drained triaxial compression with reloading (Figure 6.28), undrained triaxial compression (Figures 6.29 and 6.30), and stress path 5 (Figure 6.31). As for the previous suite of simulations, it may be concluded that the model is able to reproduce the mechanical behavior of oil-saturated chalk reasonably well. Some of the values for the model parameters obtained from the correlations may be seen to contain significant error. The most noticeable errors for this suite of tests are in the preconsolidation stress for File 319, in the critical state slope and/or eccentricity parameter for File 326, and in the eccentricity parameter for File 434.

Comparisons between the lab results and simulation results for the tests on Dan field chalk are shown in Figures 6.32 through 6.38. The simulations include hydrostatic compression (Figures 6.32), K_0 compression (Figures 6.33), drained triaxial compression (Figures 6.34 and 6.35), undrained triaxial compression (Figures 6.36 and 6.37), and stress path 5 (Figure 6.38). For Dan chalk, it becomes clear that the correlation between porosity and preconsolidation stress

significantly underestimates the actual preconsolidation stress. To obtain a better match between experimental and simulated results, the values for bulk modulus, preconsolidation stress, compression coefficient, adjusted failure shear stress ratio, and tensile strength are all obtained using the correlations for an equivalent chalk with a porosity 6% less than that measured; for example, the measured porosity for File 310 is 39.3%, but the values for the model parameters are obtained as if the porosity is 33.3%.

As for the previous simulations, it may be concluded that the model is able to reproduce the mechanical behavior of oil-saturated chalk reasonably well. Some of the values for the model parameters obtained from the correlations may be seen to contain significant error. The most noticeable errors for this suite of tests is in the preconsolidation stress for File 313 and in the cap aspect ratio for File 420.

REFERENCES

Goodman, R.E. (1989). Rock Mechanics. New York, John Wiley and Sons, 562 p.

Gutierrez, M.S. (1999). Modelling of Time-Dependent Chalk Behavior and Chalk-Water Interaction, NGI Report no. 541105-4.

William, K.J. and Warnke, E.P. (1975). Constitutive model for the triaxial behavior of concrete, ISMES Seminar on Concrete Structures Subjected to Triaxial Stress, Bergamo, Italy, 1-30.

Table 6.1. Required parameters for the rate-dependent constitutive model.

Parameter
Elastic behavior
Bulk modulus, K
Poisson's ratio, ν
Rate-dependent pore collapse behavior
Compression coefficient, λ
Reference time-line anchor, N
Critical state slope, M
Eccentricity parameter, R
*Attraction, a
Creep parameter, ψ
Minimum volumetric age, $t_{v,\min}$
Shear failure surface
Adjusted failure shear stress ratio, $\overline{\eta}_f$
*Attraction, a
Tensile failure surface
Tensile strength, p_t
Third-invariant effects
William-Warnke scaling parameter, k

*Attraction describes both rate-dependent pore collapse behavior and shear failure surface

Table 6.2. Values of required model parameters for simulations on Ekofisk A field chalk.

Parameter	File 329	File 330	File 331
Bulk modulus K (MPa)	2530	2940	1820
Poisson's ratio ν	0.24	0.24	0.24
Reference time-line anchor N	1.02	0.96	1.15
Compression coefficient λ	0.13	0.12	0.15
Cap aspect ratio M	1.14	1.35	1.10
Eccentricity parameter R	0.55	0.52	0.63
Attraction a (MPa)	4	4	4
Adjusted failure shear stress ratio $\overline{\eta}_f$	1.13	1.33	1.08
Creep parameter ψ	0.0037	0.0037	0.0037
Minimum volumetric age $t_{v,\min}$ (hours)	1	1	1
Parameter	File 332	File 335	File 341
Bulk modulus K (MPa)	2160	2080	2440
Poisson's ratio ν	0.24	0.24	0.24
Reference time-line anchor N	1.08	1.09	1.03
Compression coefficient λ	0.14	0.14	0.13
Cap aspect ratio M	1.18	1.16	1.24
Eccentricity parameter R	0.59	0.60	0.56
Attraction a (MPa)	4	4	4
Adjusted failure shear stress ratio $\overline{\eta}_f$	1.16	1.15	1.23
Creep parameter ψ	0.0037	0.0037	0.0037
Minimum volumetric age $t_{v,\min}$ (hours)	1	1	1

Table 6.3. Values of required model parameters for simulations on Valhall field chalk.

Parameter	File 318	File 319	File 320
Bulk modulus K (MPa)	3940	3760	4450
Poisson's ratio ν	0.24	0.24	0.24
Reference time-line anchor N	0.84	0.89	0.83
Compression coefficient λ	0.10	0.11	0.10
Cap aspect ratio M	1.58	1.50	1.62
Eccentricity parameter R	0.46	0.47	0.43
Attraction a (MPa)	4	4	4
Adjusted failure shear stress ratio $\overline{\eta}_f$	1.56	1.48	1.60
Creep parameter ψ	0.0037	0.0037	0.0037
Minimum volumetric age $t_{v,\min}$ (hours)	1	1	1
Parameter	File 324	File 325	File 326
Bulk modulus K (MPa)	4130	1430	1430
Poisson's ratio ν	0.24	0.24	0.24
Reference time-line anchor N	0.84	1.26	1.26
Compression coefficient λ	0.10	0.17	0.17
Cap aspect ratio M	1.56	0.99	0.99
Eccentricity parameter R	0.45	0.69	0.69
Attraction a (MPa)	4	4	4
Adjusted failure shear stress ratio $\overline{\eta}_f$	1.55	0.98	0.98
Creep parameter ψ	0.0037	0.0037	0.0037
Minimum volumetric age $t_{v,\min}$ (hours)	1	1	1
Parameter	File 327	File 434	File 440
Bulk modulus K (MPa)	1540	1480	1820
Poisson's ratio ν	0.24	0.24	0.24
Reference time-line anchor N	1.21	1.23	1.15
Compression coefficient λ	0.16	0.17	0.15
Cap aspect ratio M	1.02	1.01	1.10
Eccentricity parameter R	0.67	0.68	0.63
Attraction a (MPa)	4	4	4
Adjusted failure shear stress ratio $\overline{\eta}_f$	1.00	0.99	1.08
Creep parameter ψ	0.0037	0.0037	0.0037
Minimum volumetric age $t_{v,\min}$ (hours)	1	1	1

Table 6.4. Values of required model parameters for simulations on Dan field chalk.

Parameter	File 310	File 311	File 312	File 313
Bulk modulus K (MPa)	3760	4170	3690	4540
Poisson's ratio ν	0.24	0.24	0.24	0.24
Reference time-line anchor N	1.04	0.98	1.04	0.96
Compression coefficient λ	0.11	0.10	0.11	0.10
Cap aspect ratio M	1.50	1.57	1.49	1.63
Eccentricity parameter R	0.47	0.45	0.47	0.43
Attraction a (MPa)	4	4	4	4
Adjusted failure shear stress ratio $\overline{\eta}_f$	1.48	1.55	1.47	1.61
Creep parameter ψ	0.0037	0.0037	0.0037	0.0037
Minimum volumetric age $t_{v,\min}$ (hours)	1	1	1	1

Parameter	File 315	File 316	File 420
Bulk modulus K (MPa)	4410	4210	3900
Poisson's ratio ν	0.24	0.24	0.24
Reference time-line anchor N	0.97	0.98	1.02
Compression coefficient λ	0.10	0.10	0.11
Cap aspect ratio M	1.61	1.57	1.52
Eccentricity parameter R	0.43	0.44	0.46
Attraction a (MPa)	4	4	4
Adjusted failure shear stress ratio $\overline{\eta}_f$	1.59	1.56	1.51
Creep parameter ψ	0.0037	0.0037	0.0037
Minimum volumetric age $t_{v,\min}$ (hours)	1	1	1

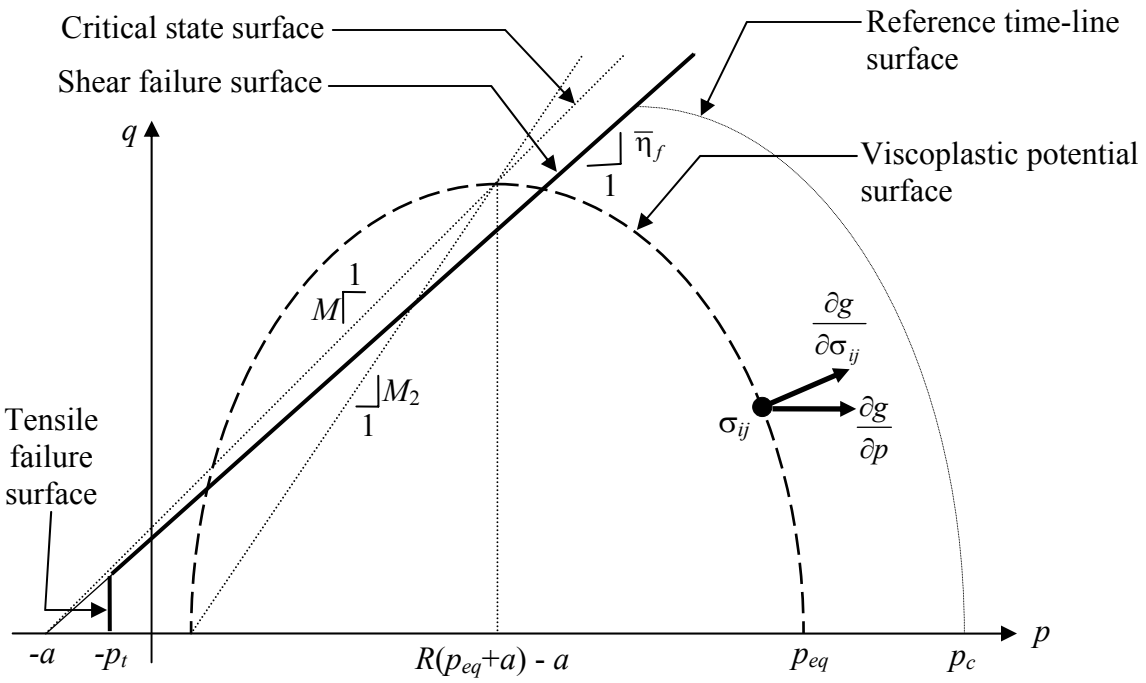

(a)

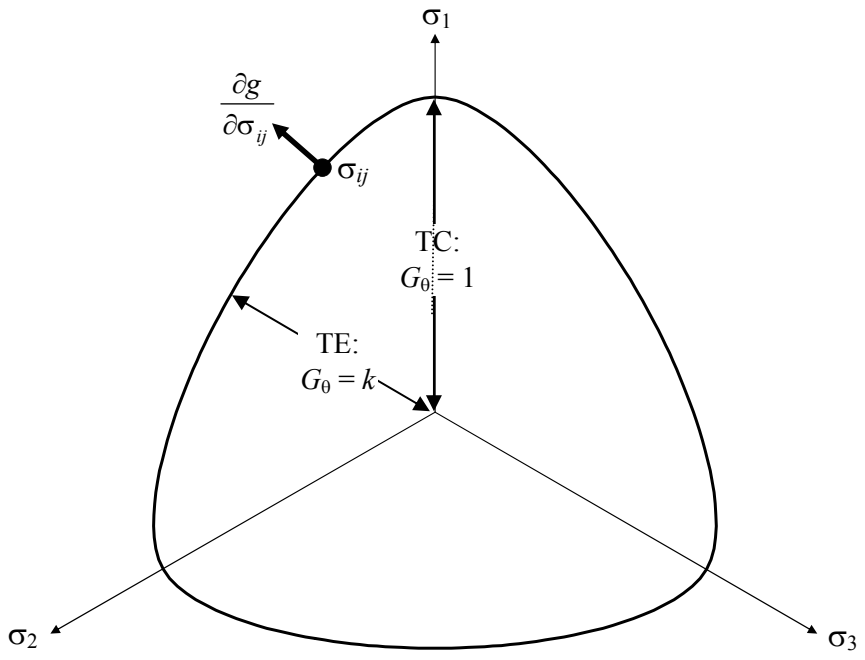

(b)

Figure 6.1. Viscoplastic potential surface and failure surfaces for the rate-dependent chalk model (a) shown in the *p-q* plane; (b) shown in the π-plane (William-Warnke surface).

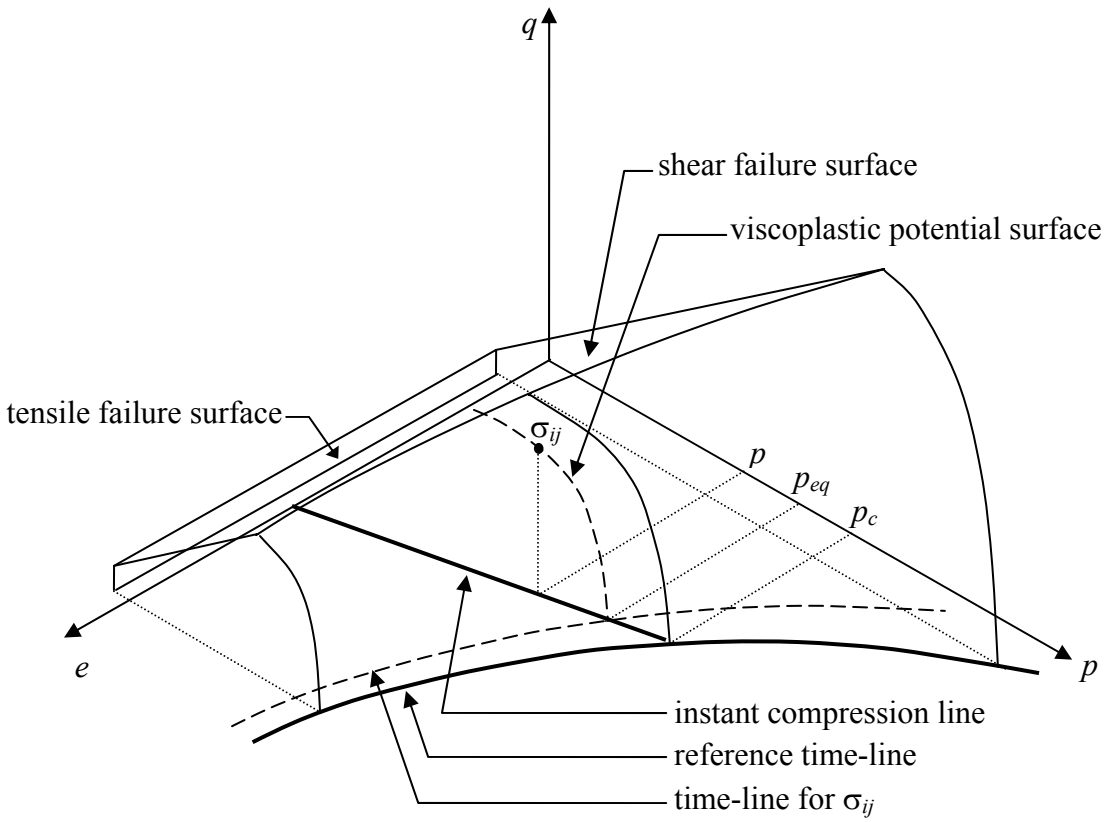

(c)

Figure 6.1 (continued). Viscoplastic potential surface and failure surfaces for the rate-dependent chalk model (c) shown in *p*-*q*-*e* space.

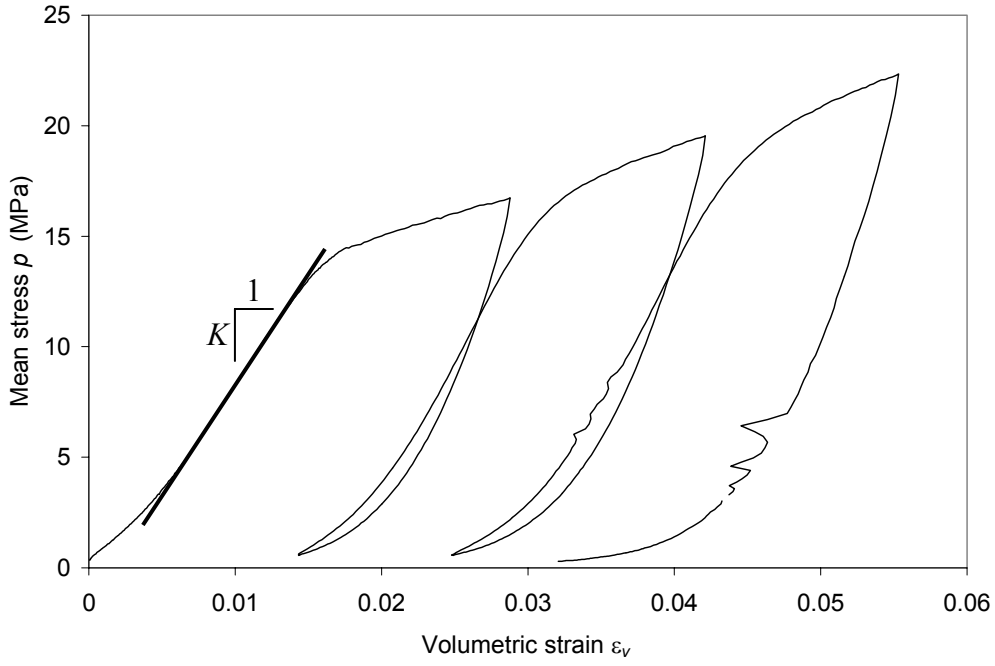

(a)

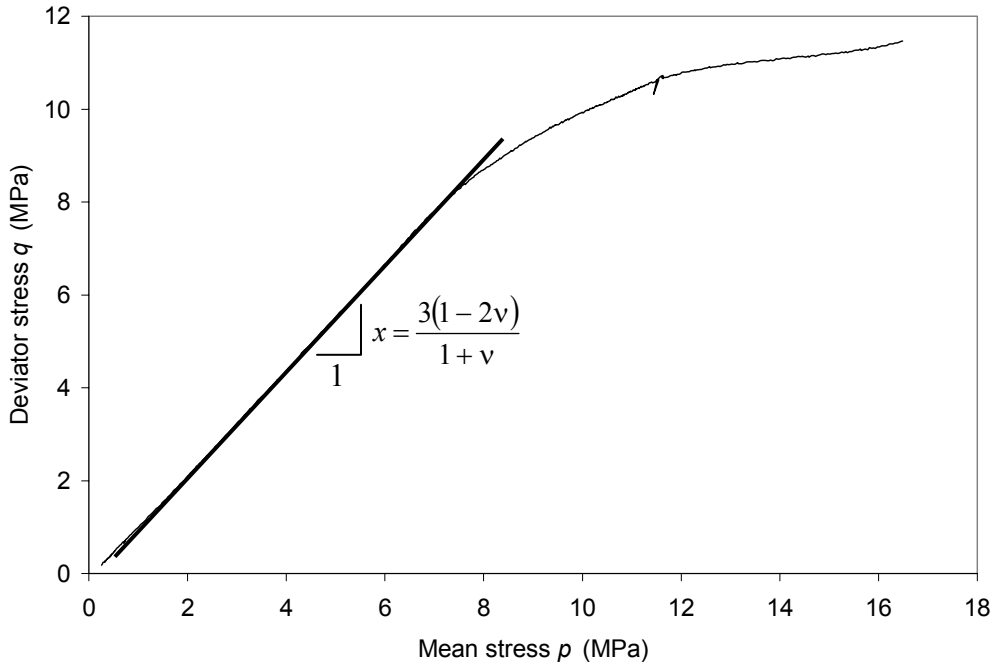

(b)

Figure 6.2. Determination of elastic coefficients required for the chalk model: (a) bulk modulus *K* from hydrostatic compression test data and (b) Poisson's ratio ν from K_0 compression test data. Data shown is from Valhall field (Files 325 and 326).

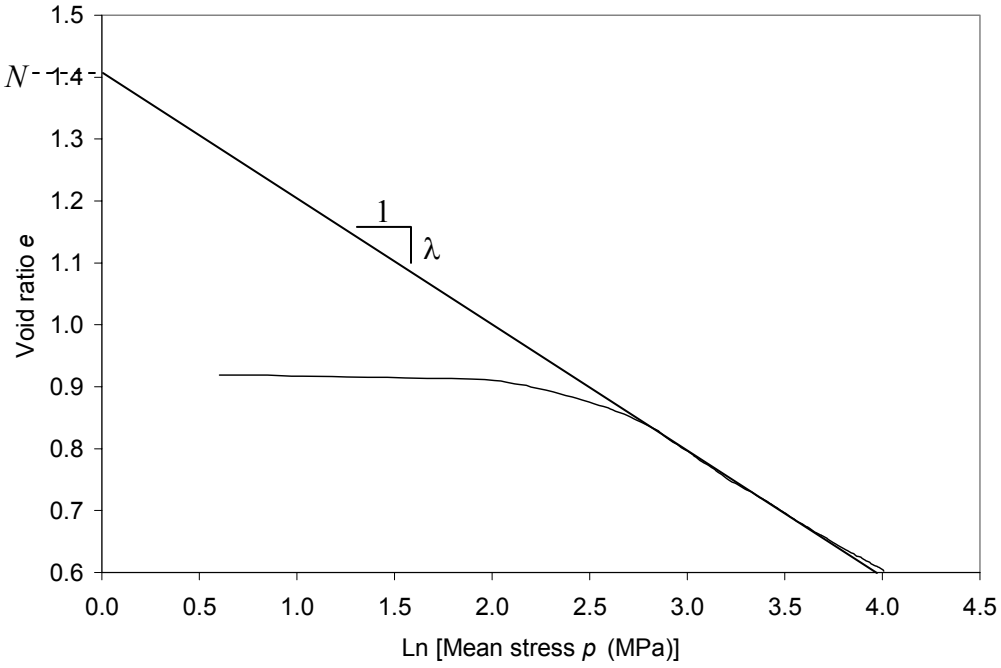

Figure 6.3. Determination of compression parameters (compression coefficient λ and reference time-line anchor *N*) from hydrostatic compression test data. Data shown is from Stevns Klint outcrop (File 26).

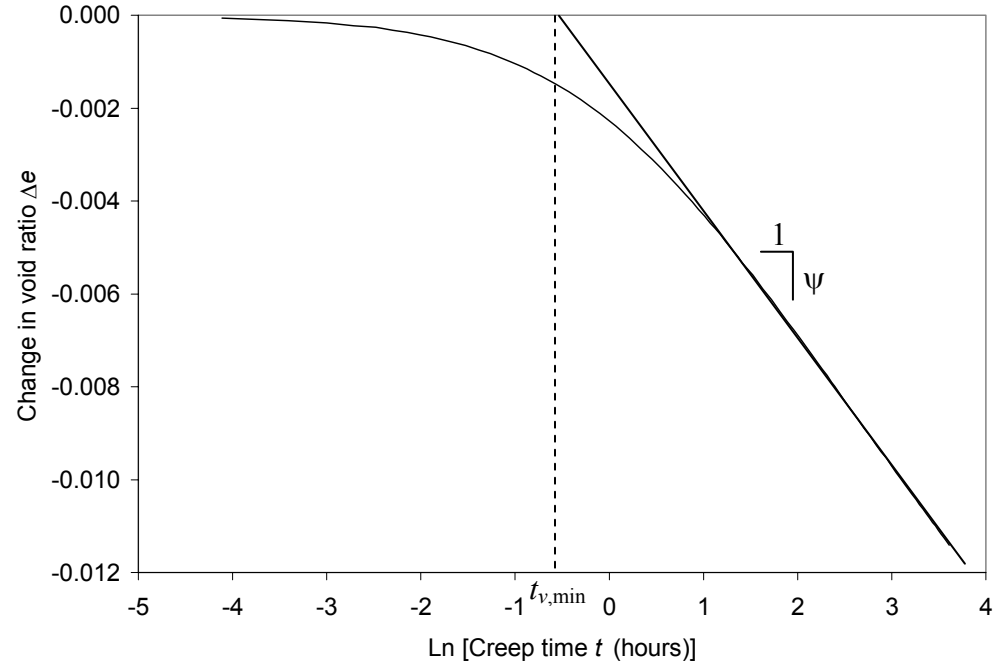

Figure 6.4. Determination of rate-dependent parameters (creep parameter ψ and minimum volumetric age $t_{v,\min}$) from σ-constant creep test data under K_0 compression conditions. Data shown is from Tyra field (File 454).

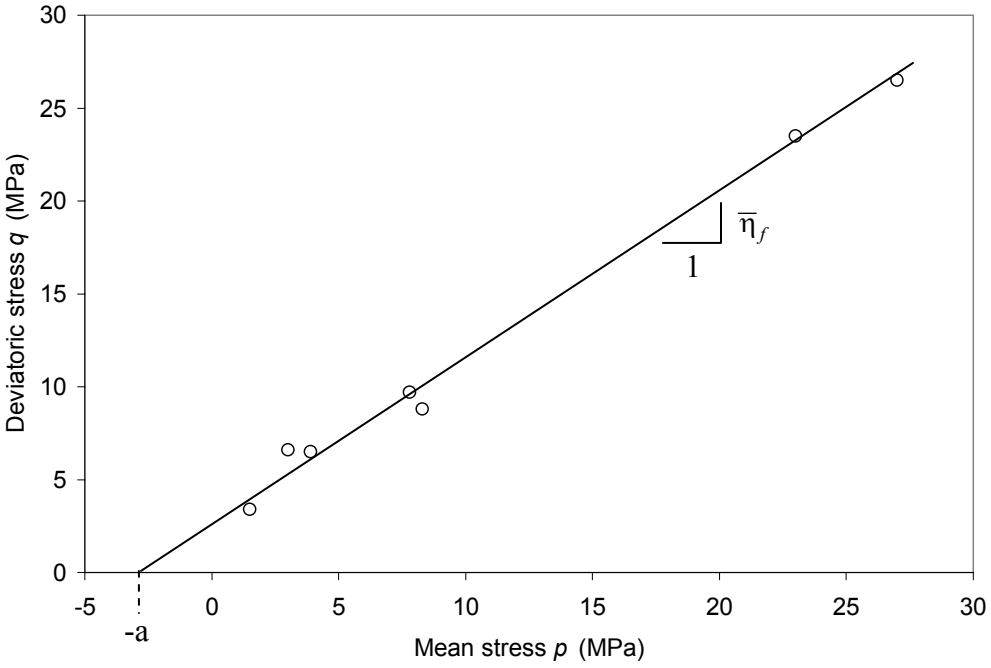

Figure 6.5. Determination of shear strength parameters (adjusted failure shear stress ratio $\overline{\eta}_f$ and attraction *a*) from triaxial compression test data. Data shown is from Butser-Hill outcrop.

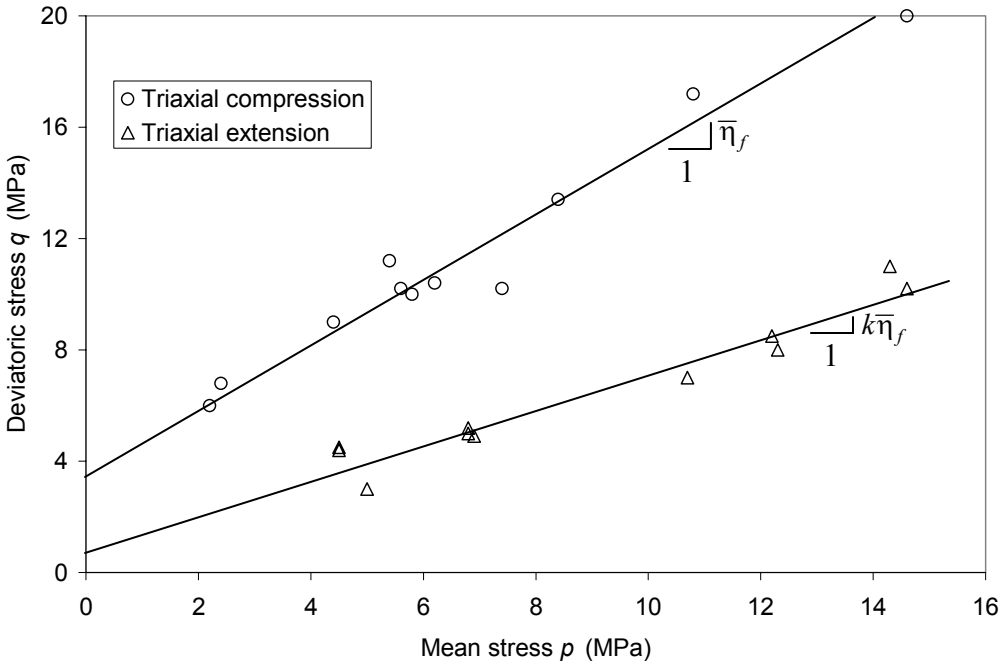

Figure 6.6. Determination of third-invariant parameter (William-Warnke scaling parameter *k*) from triaxial compression and triaxial extension test data. Data shown is from Lixhe outcrop (triaxial compression data from Collin et al., 2002).

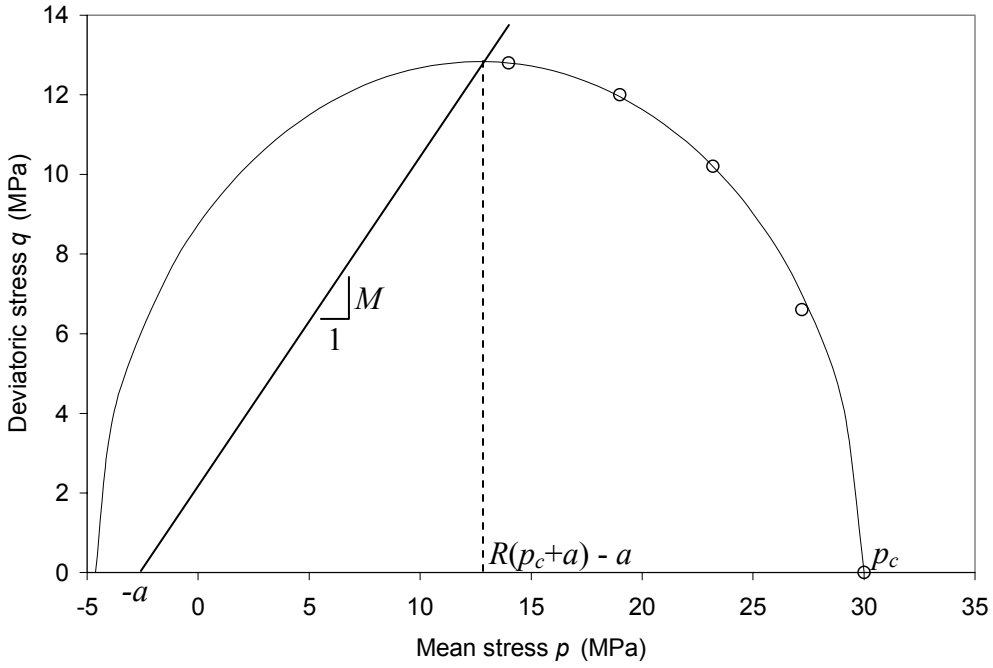

(a)

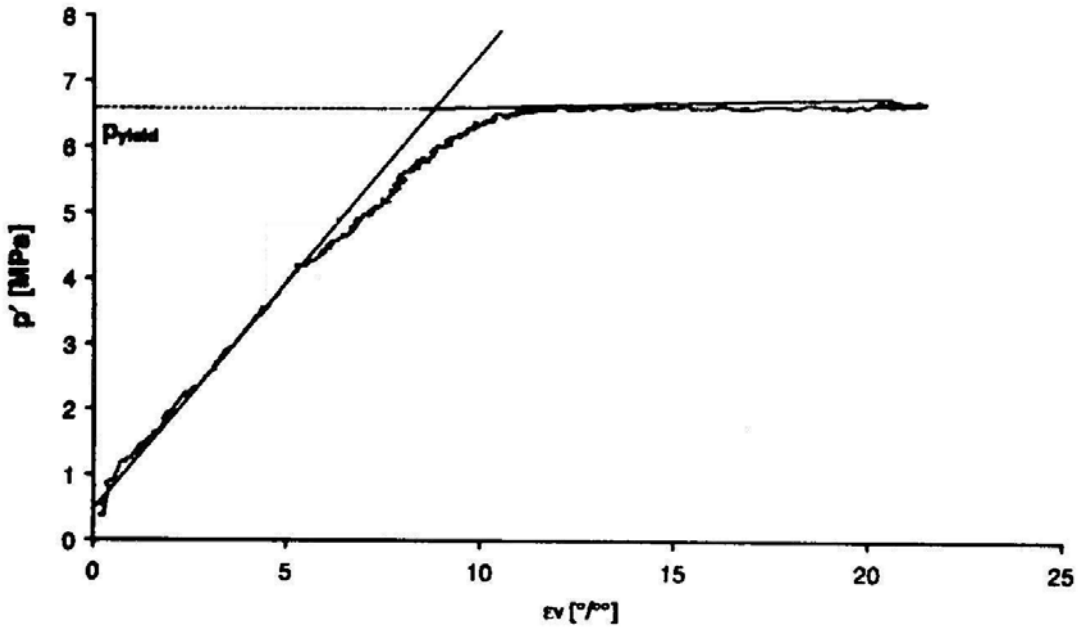

(b)

Figure 6.7. Determination of elliptical cap parameters (critical state slope *M* and eccentricity parameter *R*) from triaxial compression test data. Best-fit parabola is shown in (a); yield point is determined as shown in (b). Data shown is from Lixhe outcrop (Collin et al., 2002).

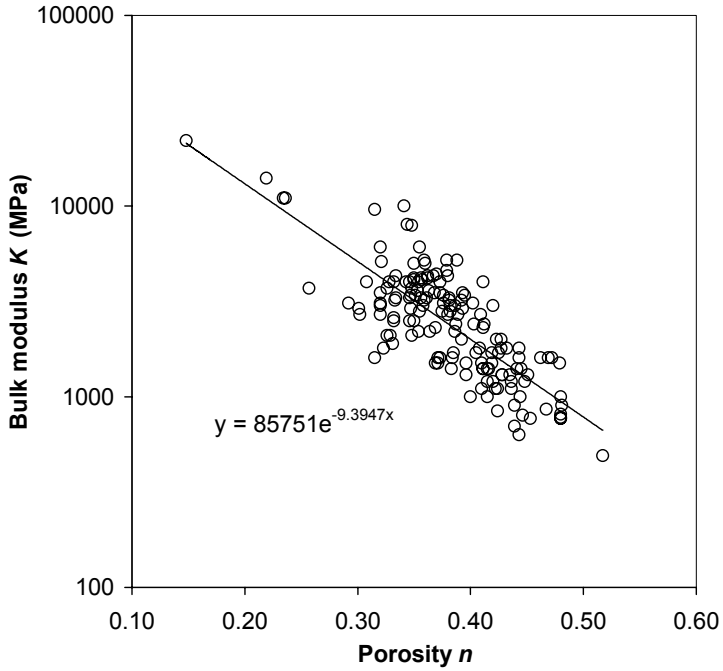

Figure 6.8. Correlation between porosity *n* and bulk modulus *K* for oil- and gas-saturated chalks. Lower-porosity North Sea chalks have greater bulk modulus and thus are stiffer.

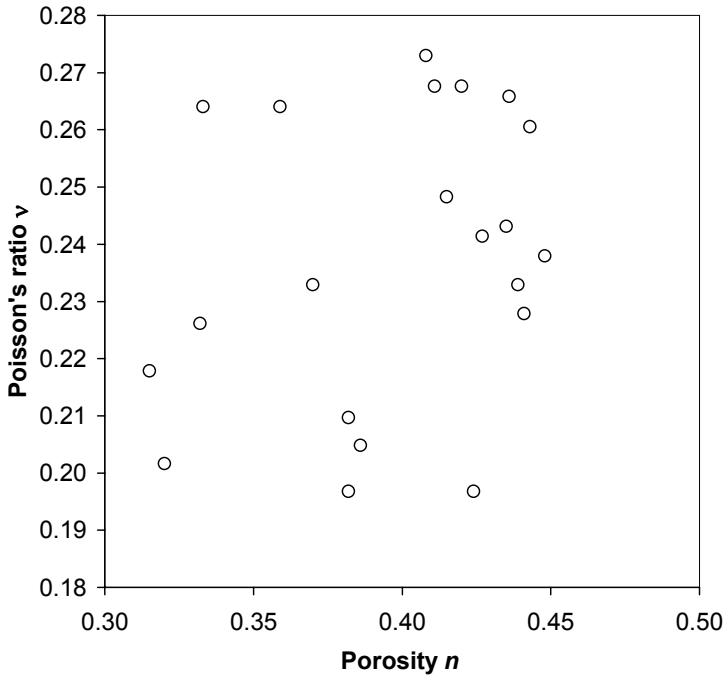

Figure 6.9. Poisson's ratio ν falls within a narrow range for North Sea oil-saturated chalks, but does not vary systematically with porosity.

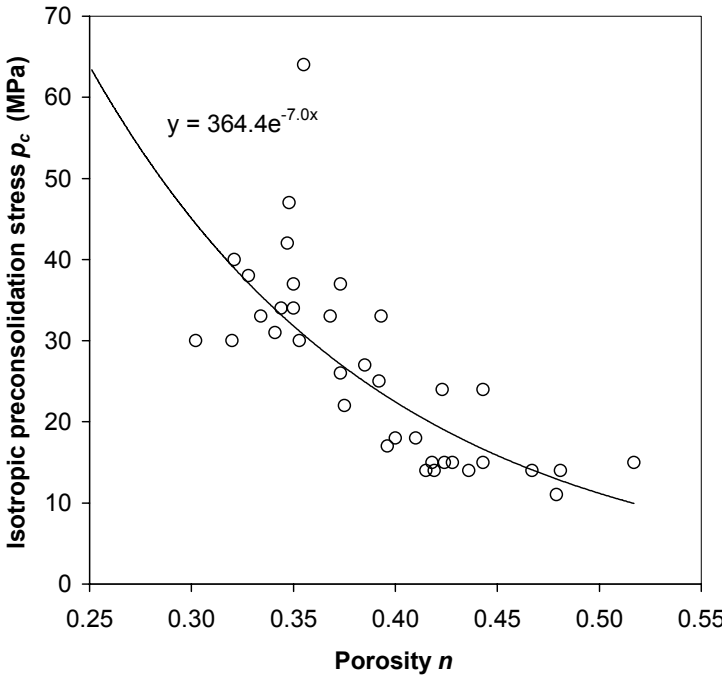

Figure 6.10. Correlation between porosity n and preconsolidation stress p_c for oil-saturated chalks. Lower-porosity North Sea chalks undergo pore collapse at a greater preconsolidation stress.

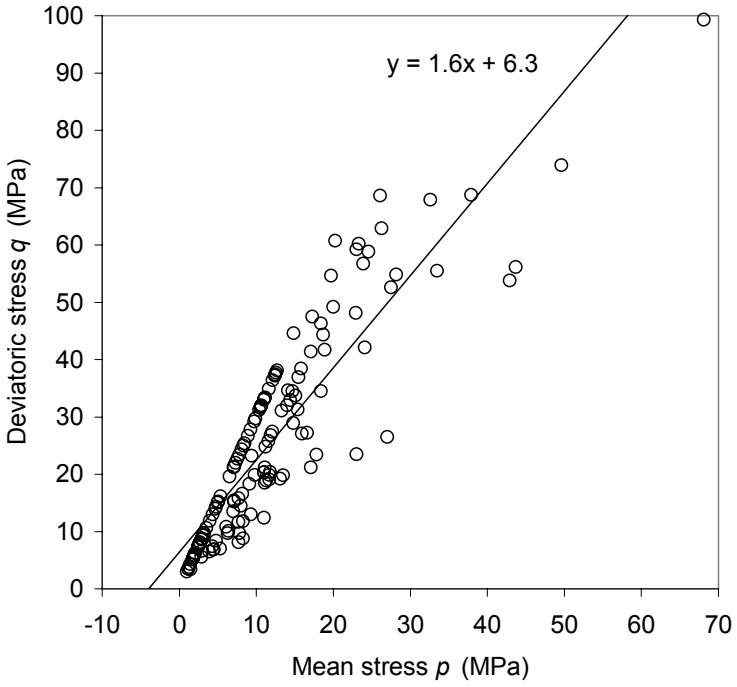

(a)

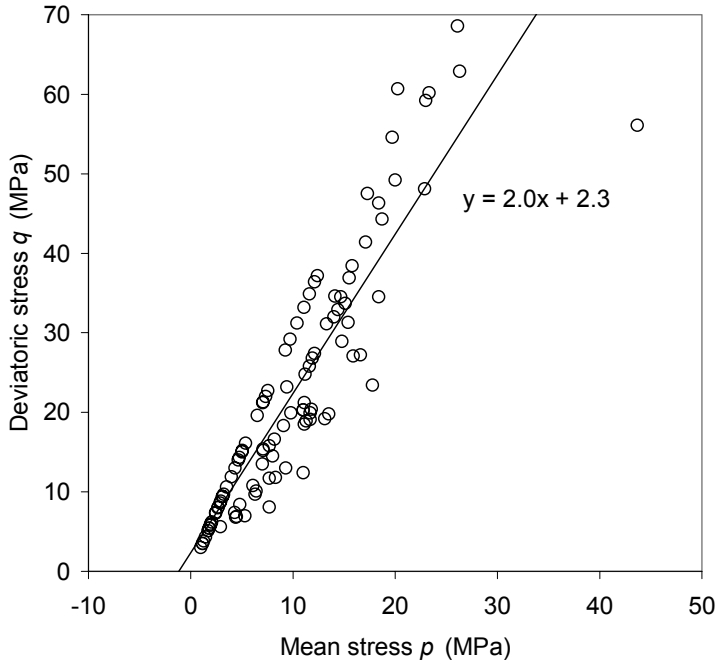

(b)

Figure 6.11. Attraction *a* for composite yield envelope for (a) all North Sea chalks is approximately 4 MPa, but (b) decreases to 1.2 MPa if only deep-sea chalks are considered.

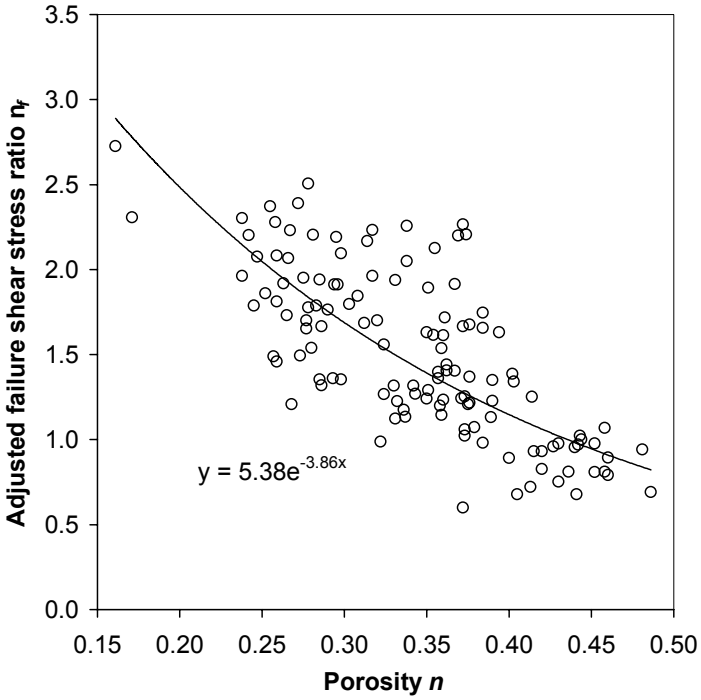

(a)

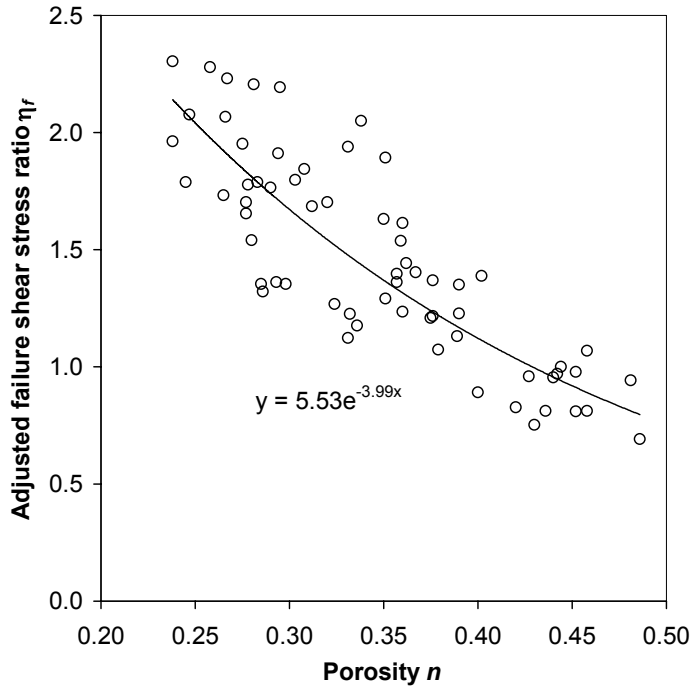

(b)

Figure 6.12. Correlation between porosity *n* and adjusted failure shear stress ratio $\overline{\eta}_f$ for (a) all oil- and gas-saturated chalks, in both triaxial compression and unconfined compression; (b) deep-sea oil- and gas-saturated chalks only, in triaxial compression. Lower-porosity North Sea chalks fail at a greater shear stress ratio.

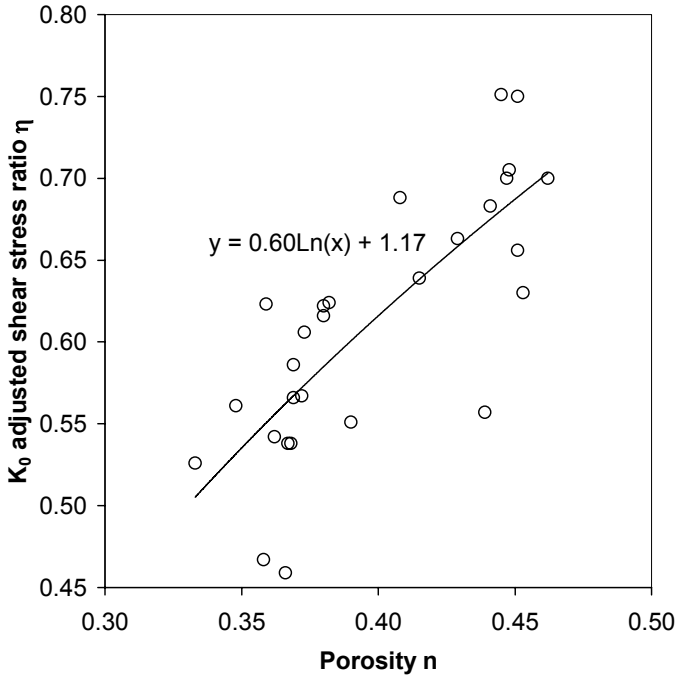

Figure 6.13. Correlation between porosity *n* and K_0 adjusted shear stress ratio $\overline{\eta}_{K_0}$ in K_0 compression. Lower-porosity North Sea chalks undergo K_0 compression at a lesser shear stress ratio, and therefore a greater relative lateral stress or K_0 value.

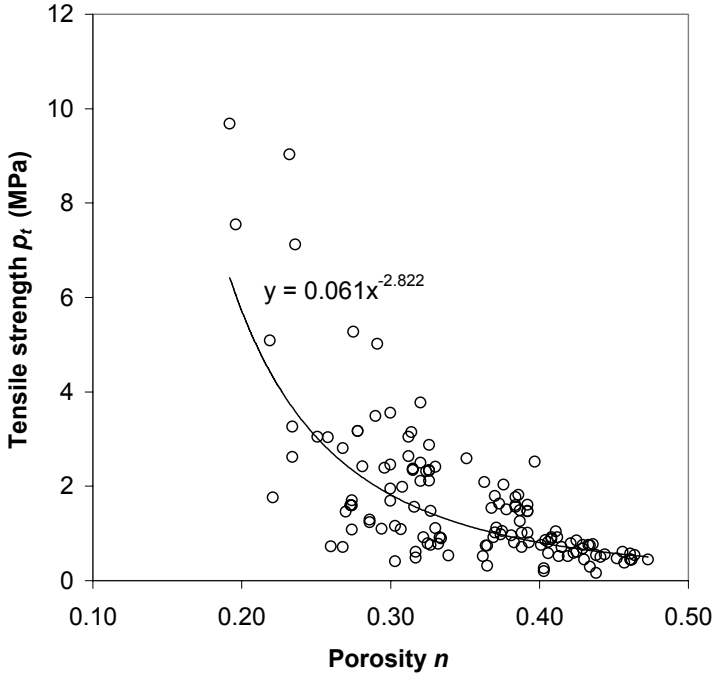

Figure 6.14. Correlation between porosity *n* and tensile strength p_t. Lower-porosity North Sea chalks fail at a greater tensile stress in Brazilian (splitting tension) tests.

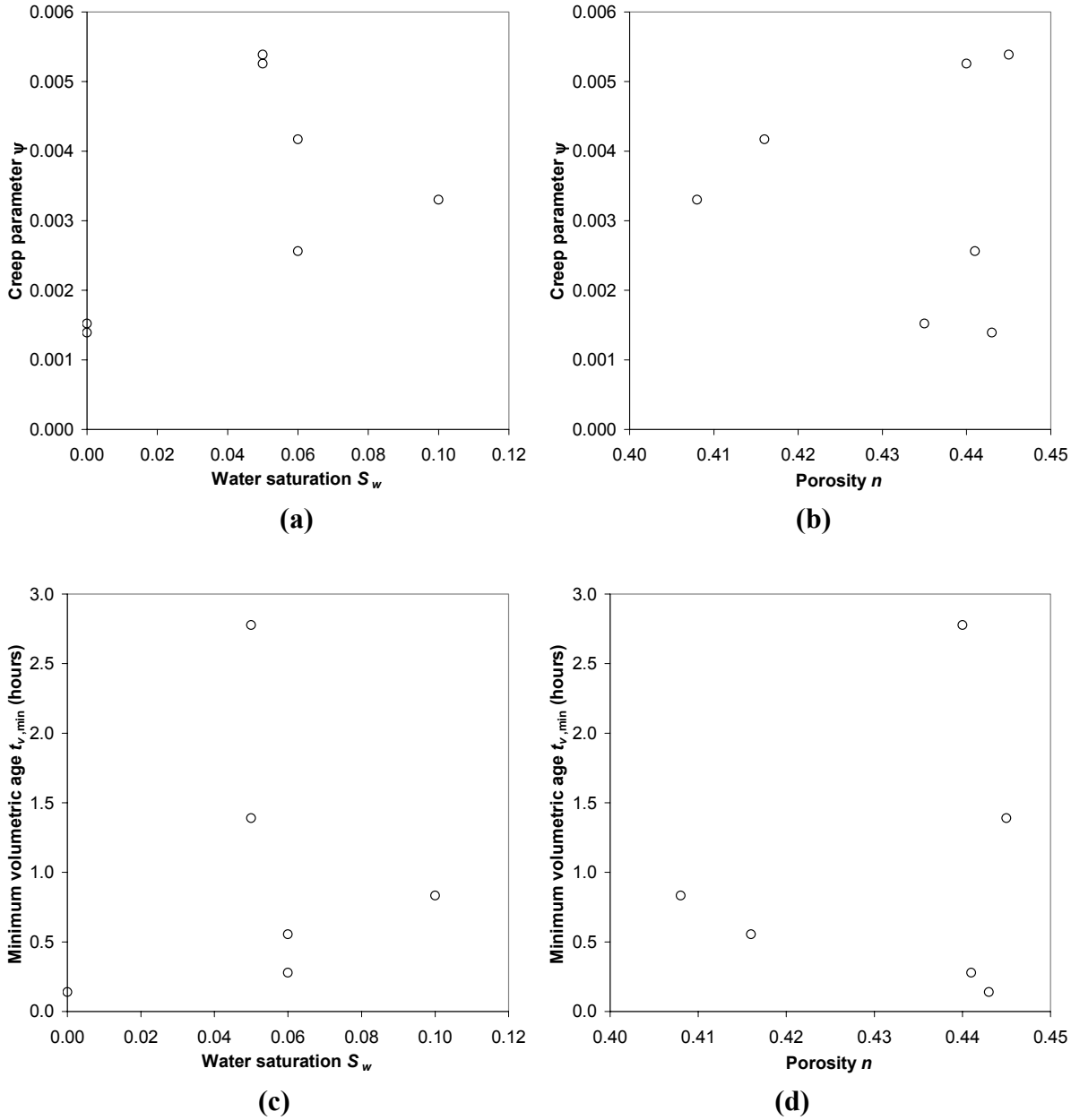

Figure 6.15. For oil-saturated chalk, the values of (a, b) creep parameter ψ and (c, d) minimum volumetric age $t_{v,\min}$ show no correlation with water saturation or porosity.

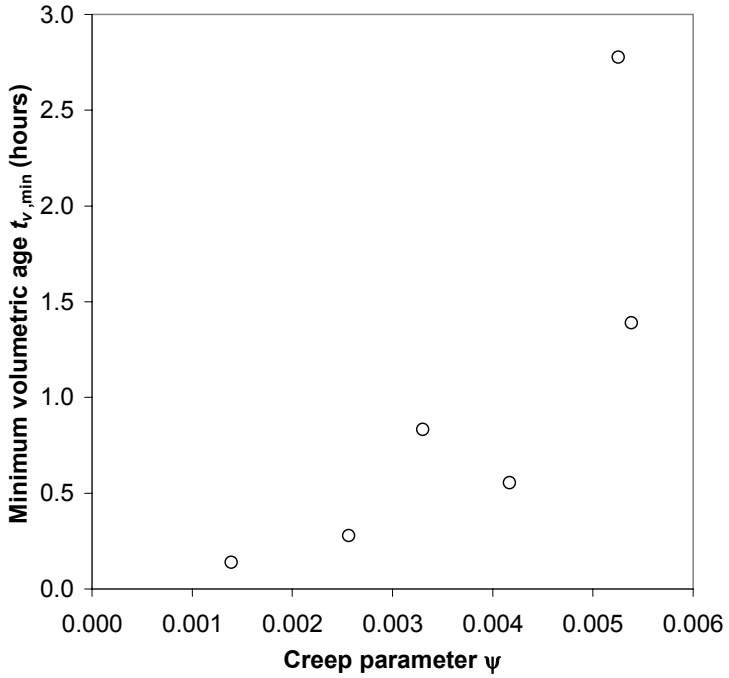

Figure 6.16. For oil-saturated chalk, a positive correlation appears to exist between the creep parameter ψ and minimum volumetric age $t_{v,min}$.

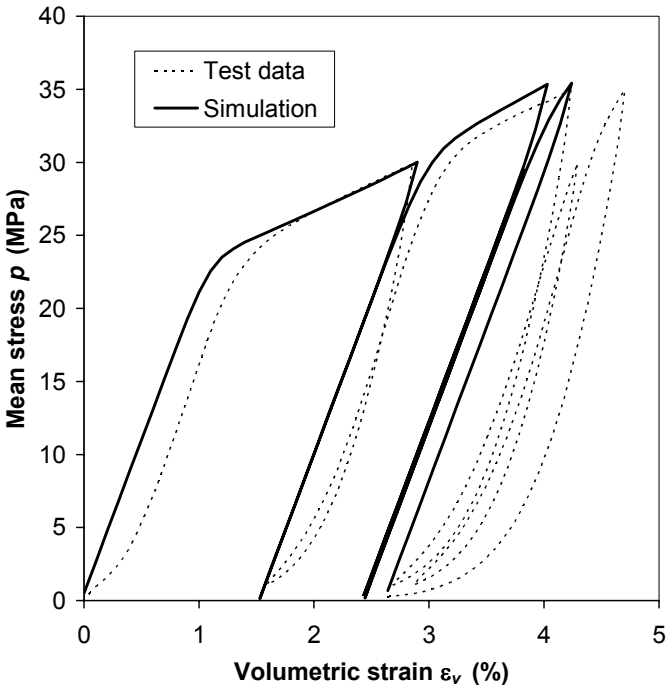

Figure 6.17. Experimental and simulated stress-strain curves for Ekofisk A chalk under cycled hydrostatic compression (File 329).

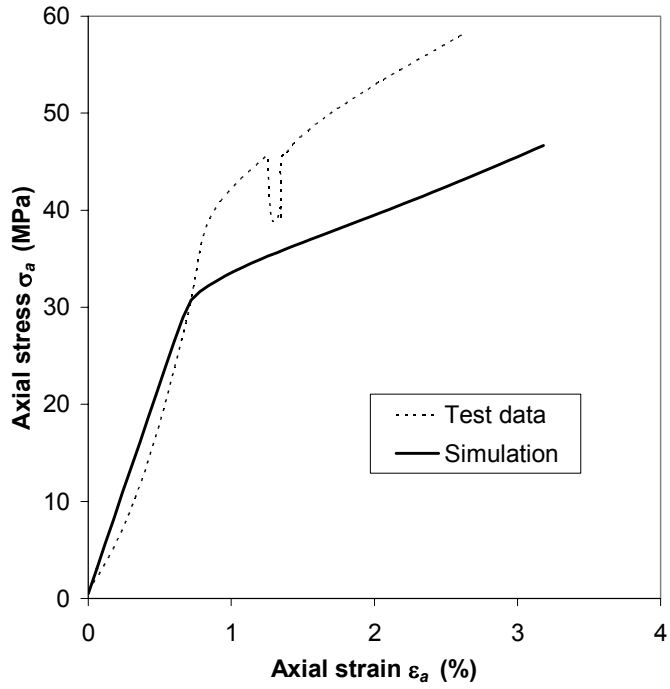

(a)

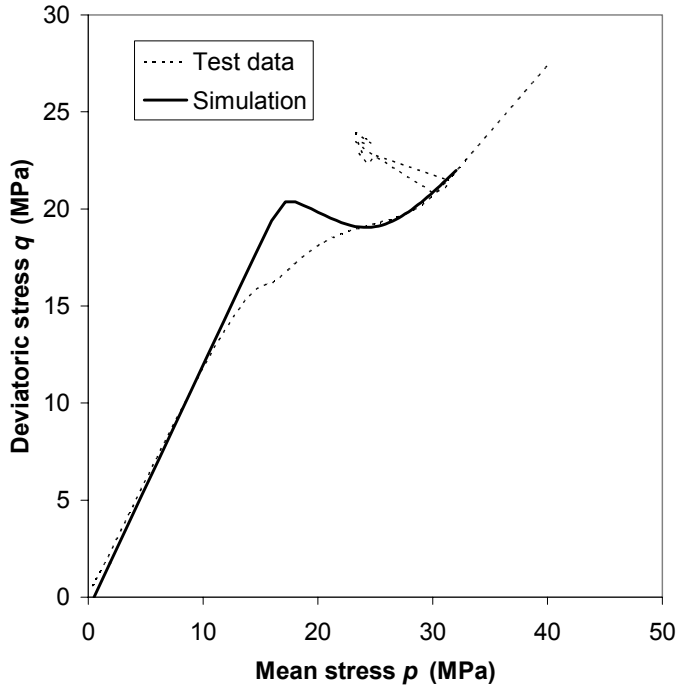

(b)

Figure 6.18. Experimental and simulated (a) stress-strain curves and (b) stress paths for Ekofisk A chalk under K_0 compression (File 330).

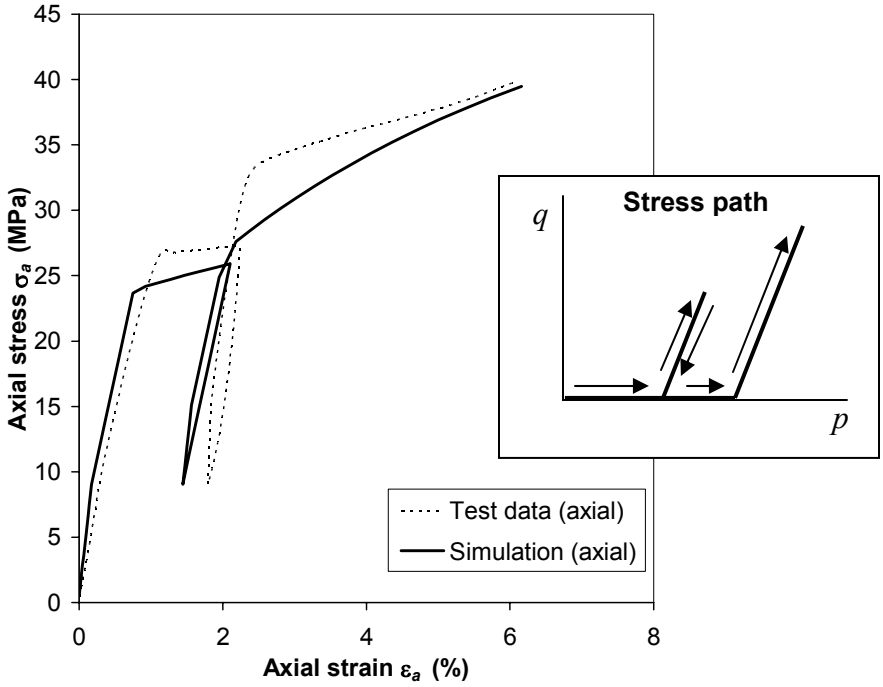

(a)

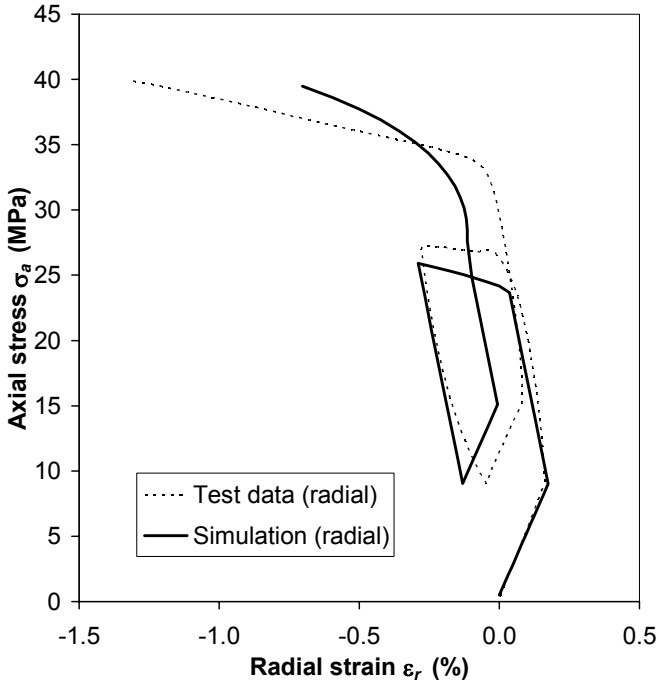

(b)

Figure 6.19. Experimental and simulated (a) axial and (b) radial stress-strain curves for Ekofisk A chalk under drained triaxial compression (File 331). Stress path shown in inset.

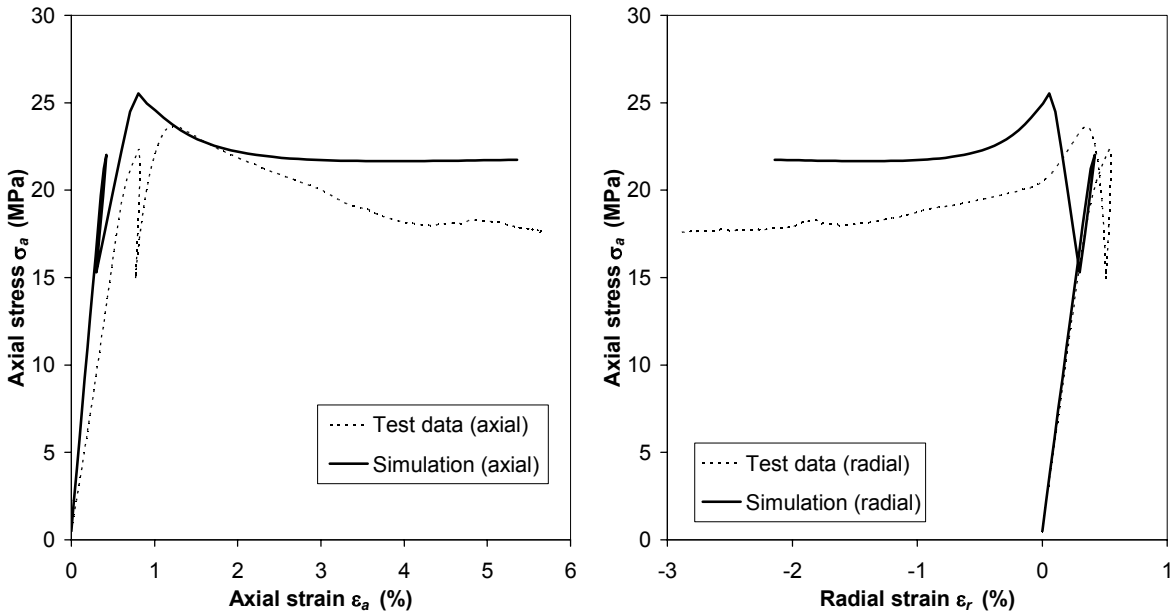

(a) **(b)**

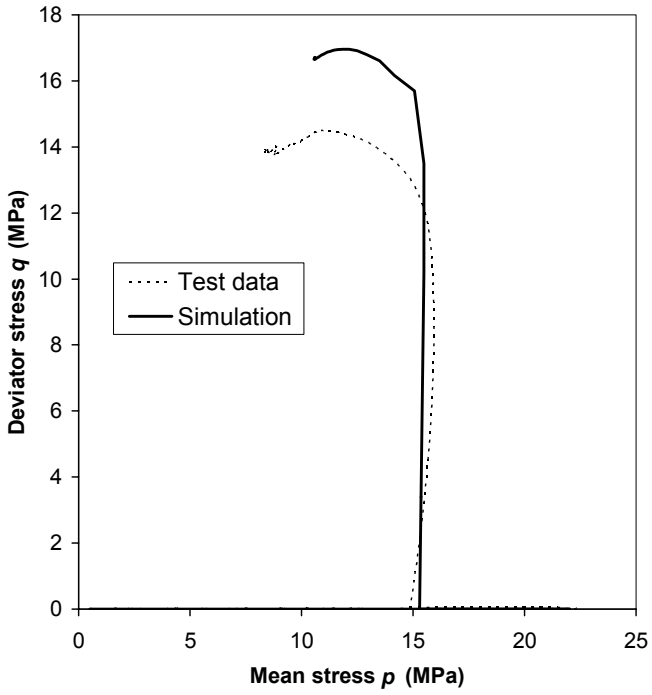

(c)

Figure 6.20. Experimental and simulated (a) axial and (b) radial stress-strain curves, and (c) stress paths for Ekofisk A chalk during overconsolided, undrained triaxial compression (File 335).

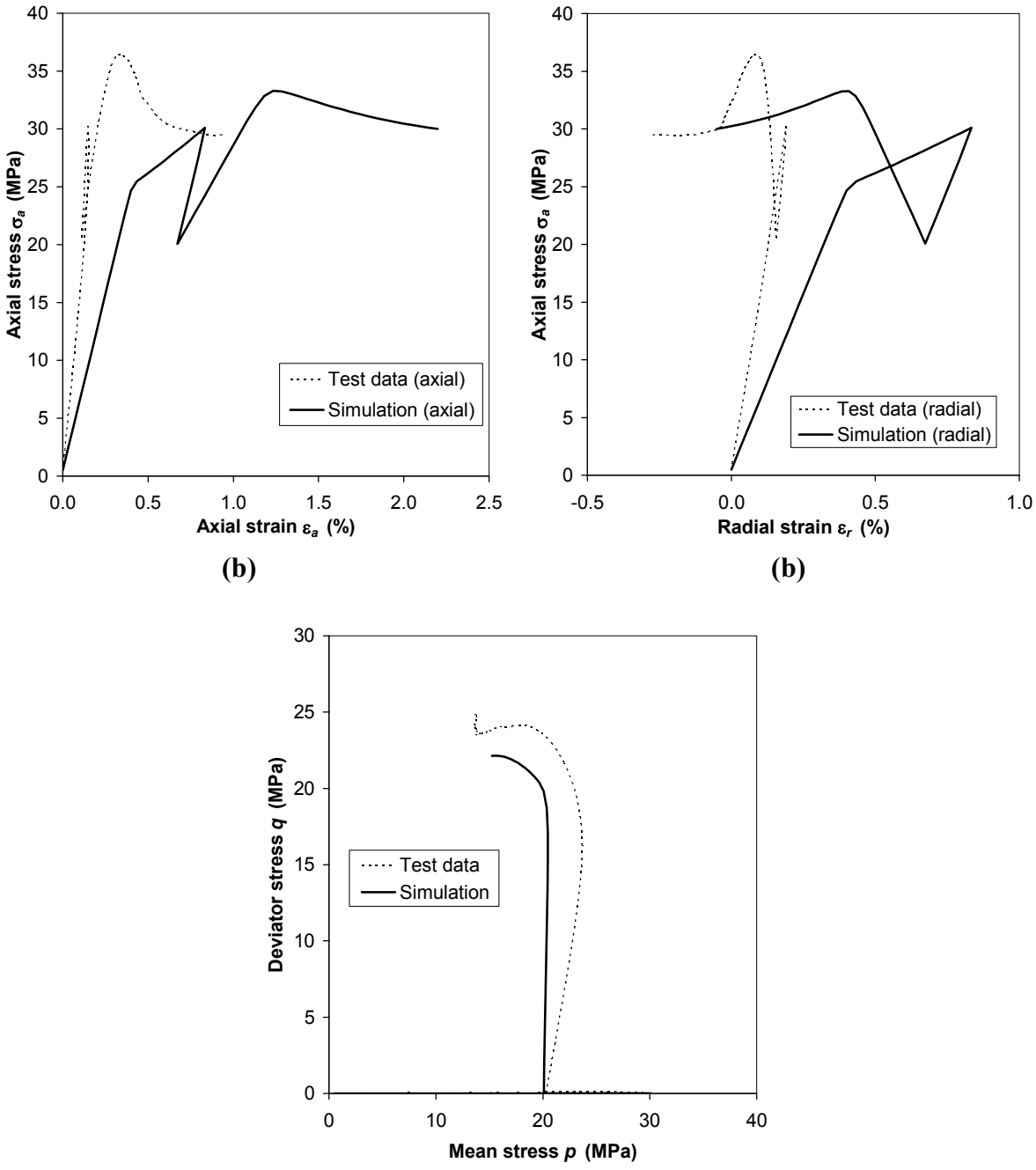

Figure 6.21. Experimental and simulated (a) axial and (b) radial stress-strain curves, and (c) stress paths for Ekofisk A chalk under overconsolided, undrained triaxial compression (File 341).

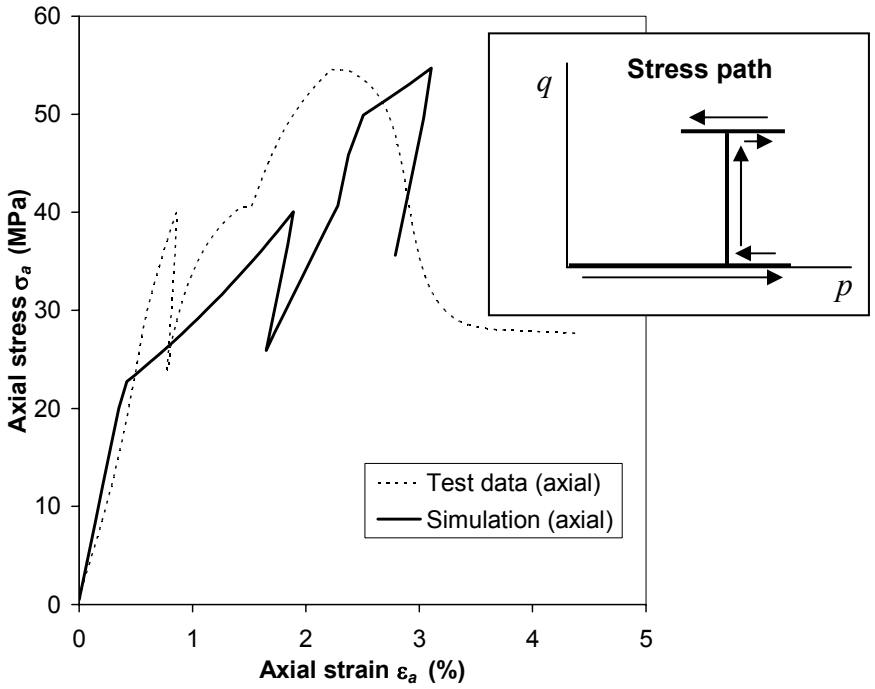

(a)

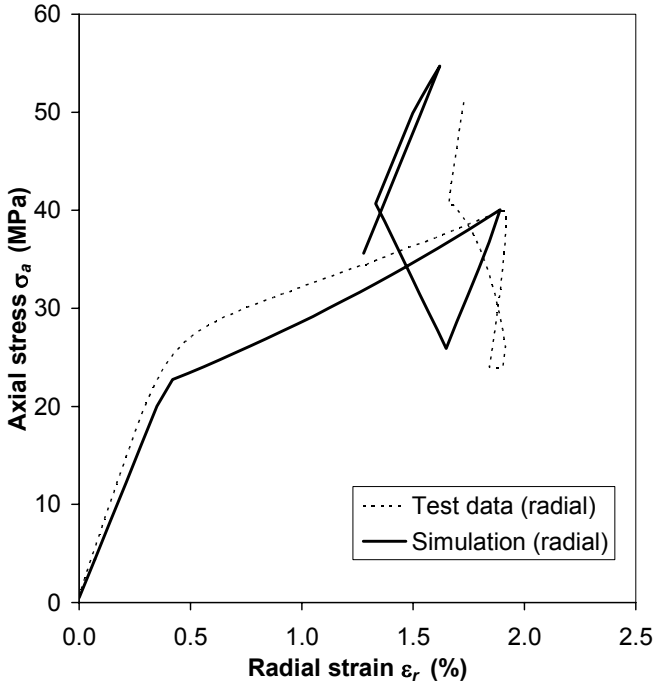

(b)

Figure 6.22. Experimental and simulated (a) axial and (b) radial stress-strain curves for Ekofisk A chalk under Stress Path 5 loading (File 332). Stress path shown to right.

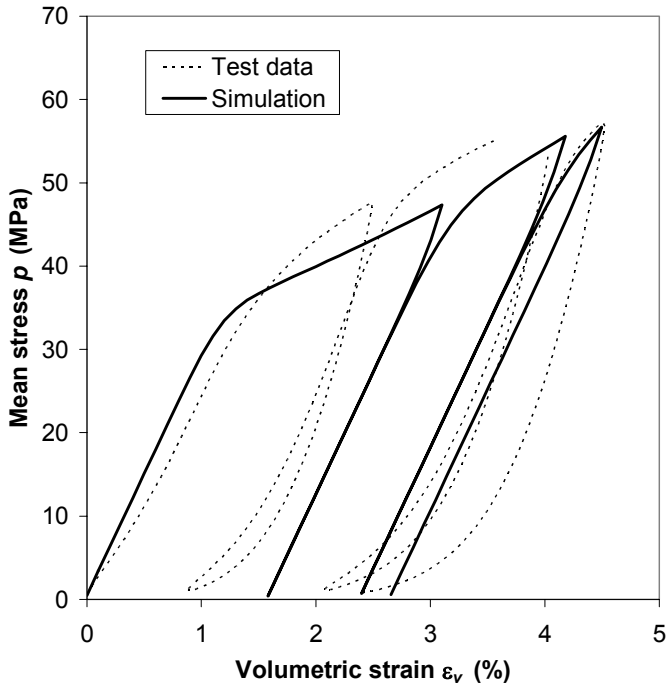

Figure 6.23. Experimental and simulated stress-strain curves for Valhall (Hod 1 Fm.) chalk under cycled hydrostatic compression (File 318).

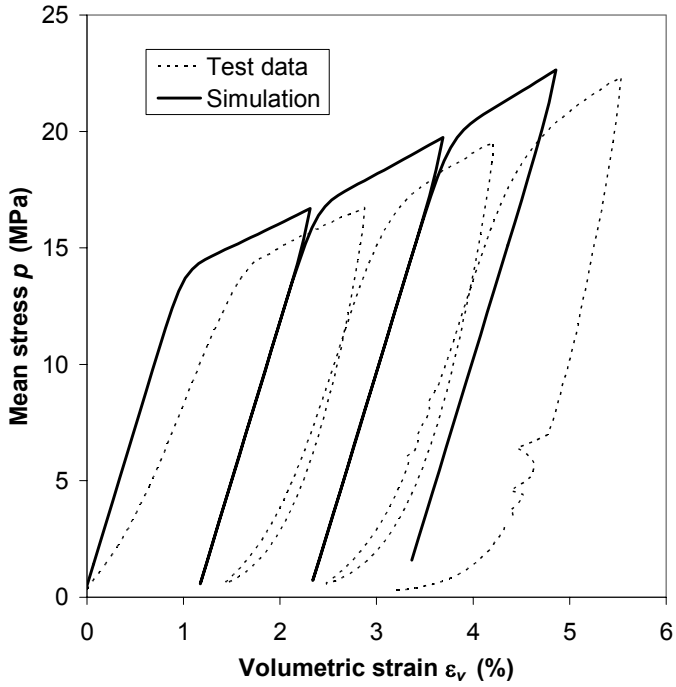

Figure 6.24. Experimental and simulated stress-strain curves for Valhall (Tor Fm.) chalk under cycled hydrostatic compression (File 325).

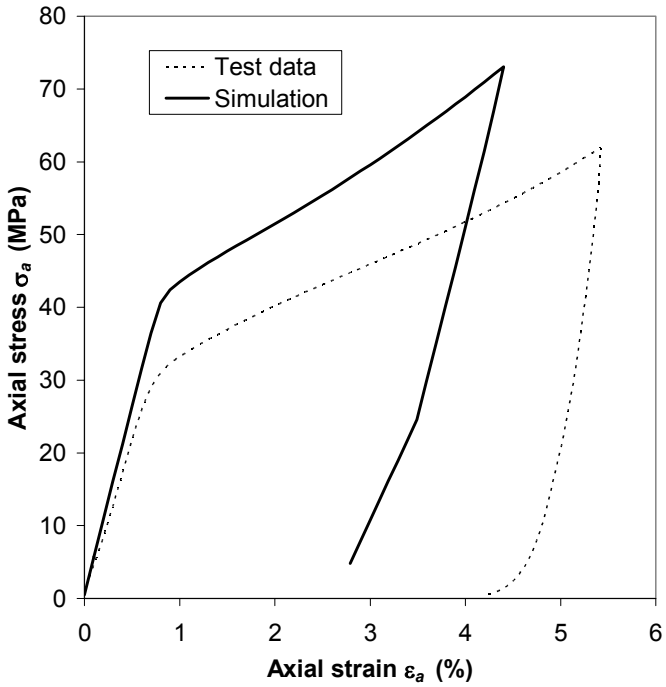

(a)

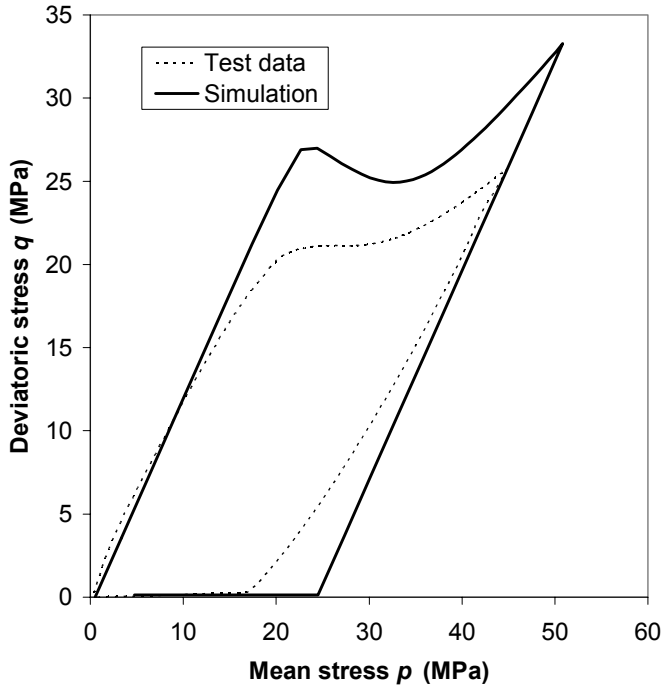

(b)

Figure 6.25. Experimental and simulated (a) stress-strain curves and (b) stress paths for Valhall (Hod 1 Fm.) chalk under K_0 compression (File 319).

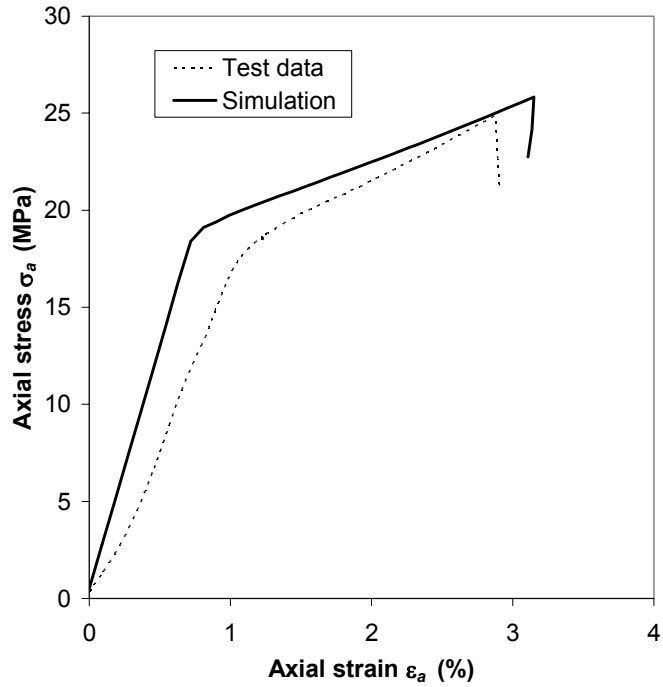

(a)

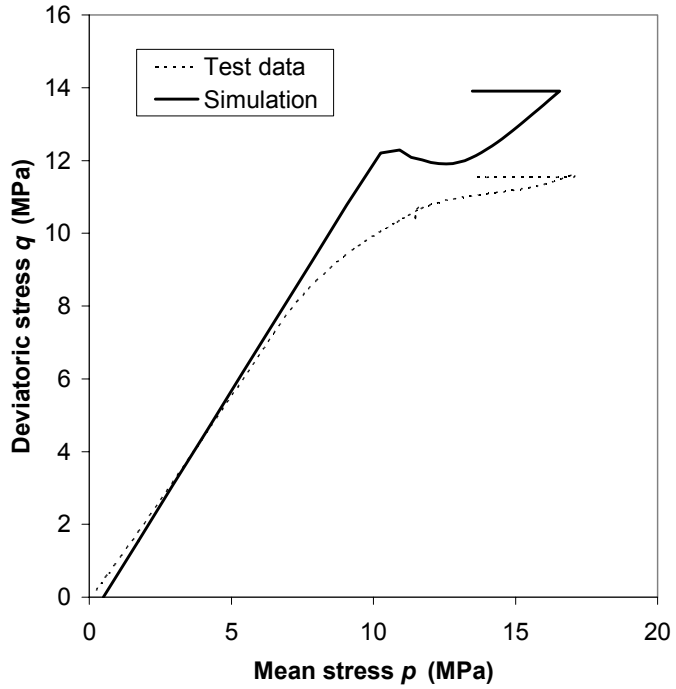

(b)

Figure 6.26. Experimental and simulated (a) stress-strain curves and (b) stress paths for Valhall (Tor Fm.) chalk under K_0 compression (File 326).

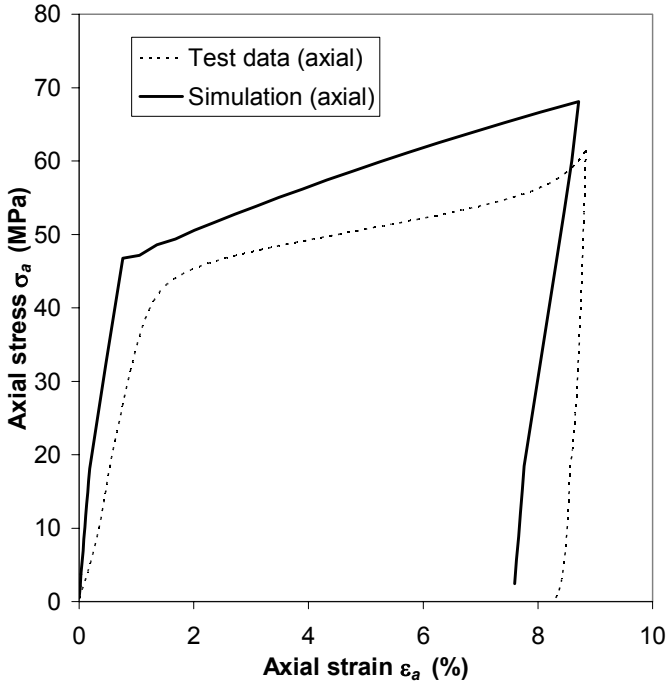

(a)

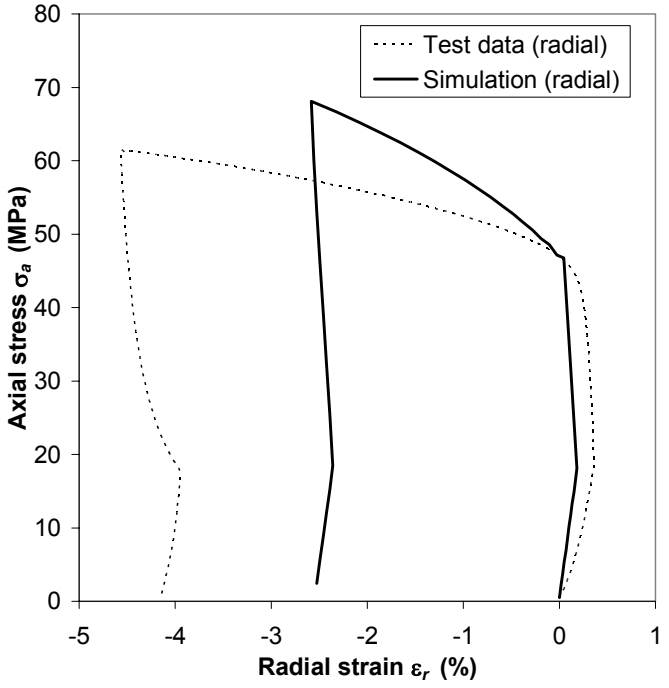

(b)

Figure 6.27. Experimental and simulated (a) axial and (b) radial stress-strain curves for Valhall (Hod 1 Fm.) chalk under drained triaxial compression (File 320).

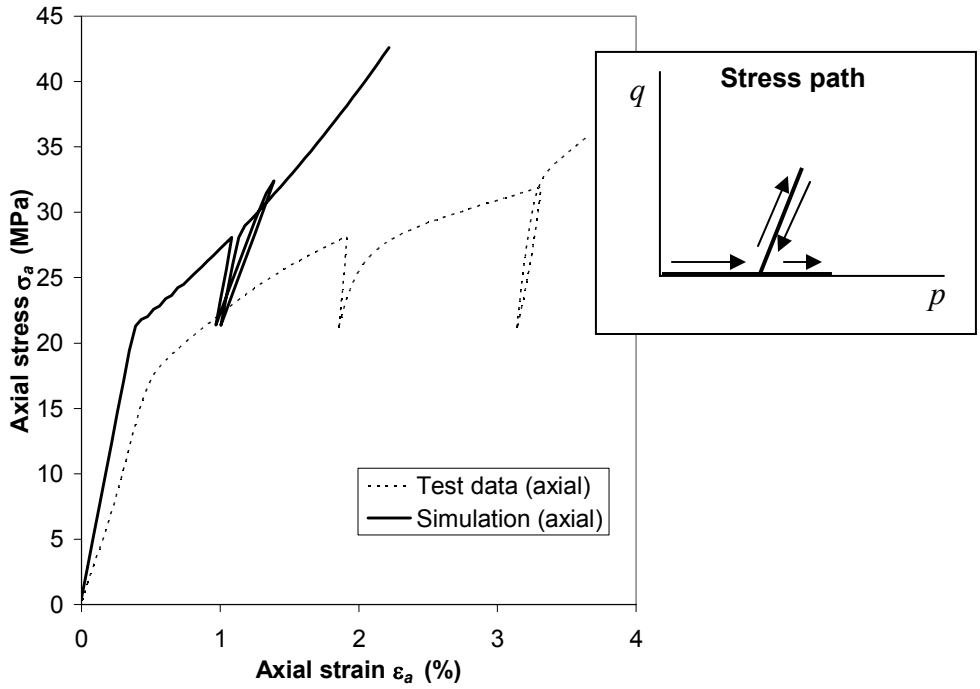

(a)

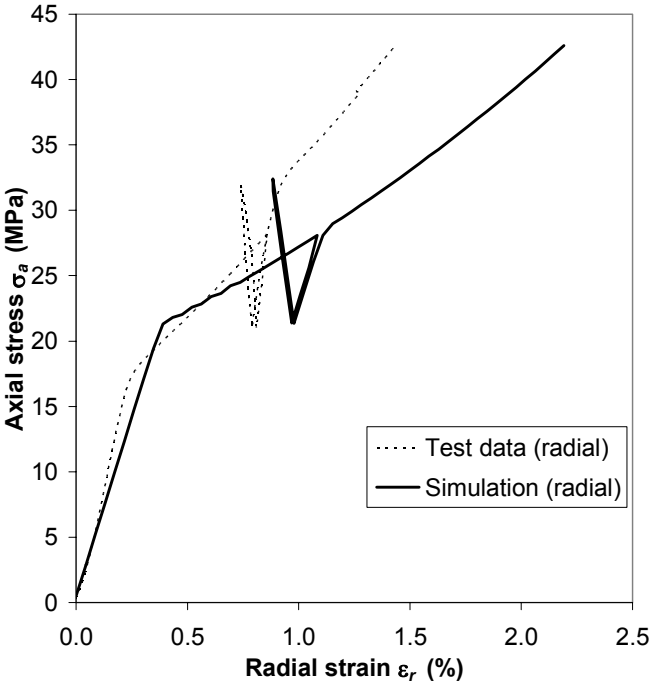

(b)

Figure 6.28. Experimental and simulated (a) axial and (b) radial stress-strain curves for Valhall (Tor Fm.) chalk under drained triaxial compression with reloading (File 440). Stress path shown in inset.

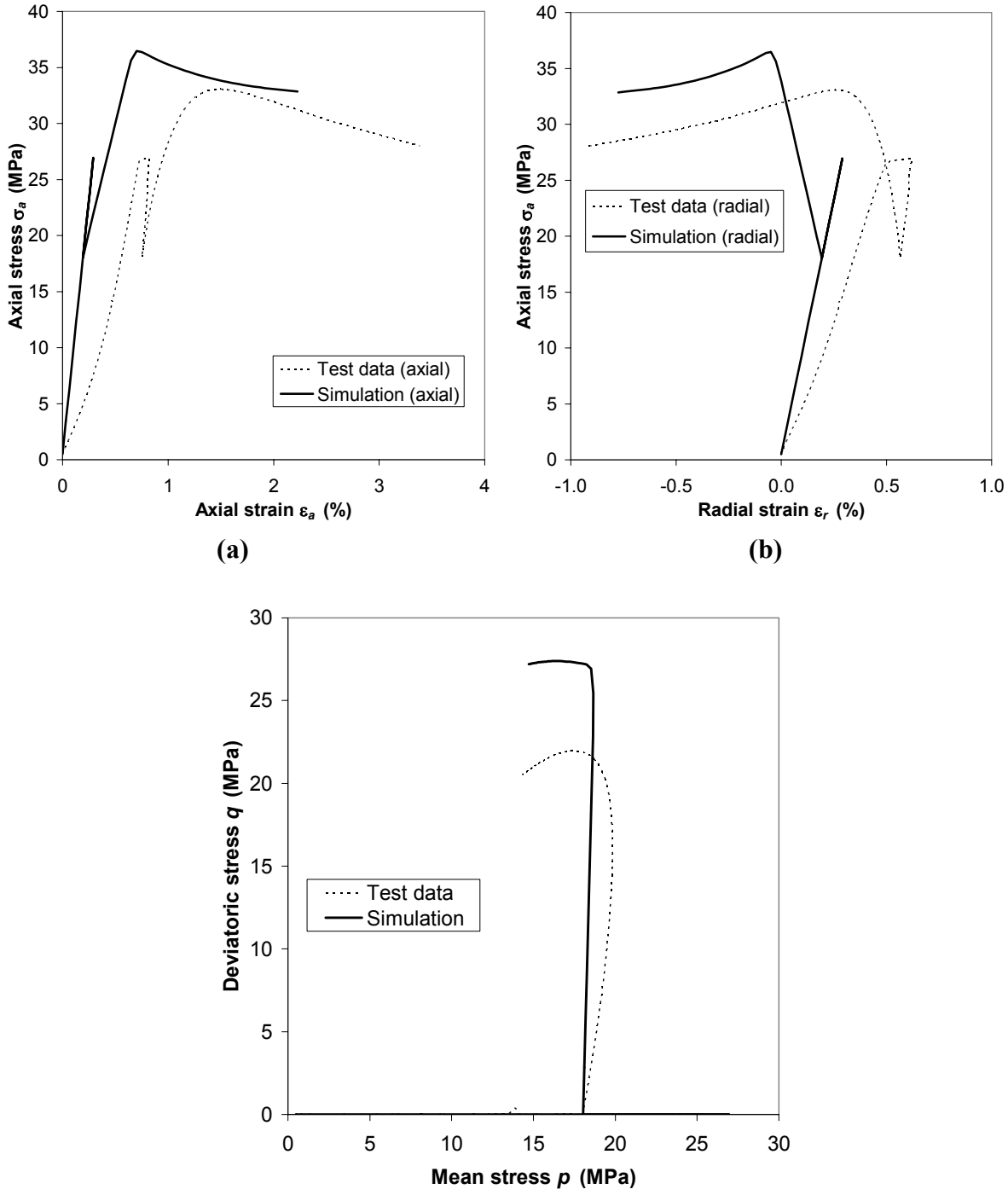

Figure 6.29. Experimental and simulated (a) axial and (b) radial stress-strain curves, and (c) stress paths for Valhall (Hod 1 Fm.) chalk during overconsolided, undrained triaxial compression (File 324).

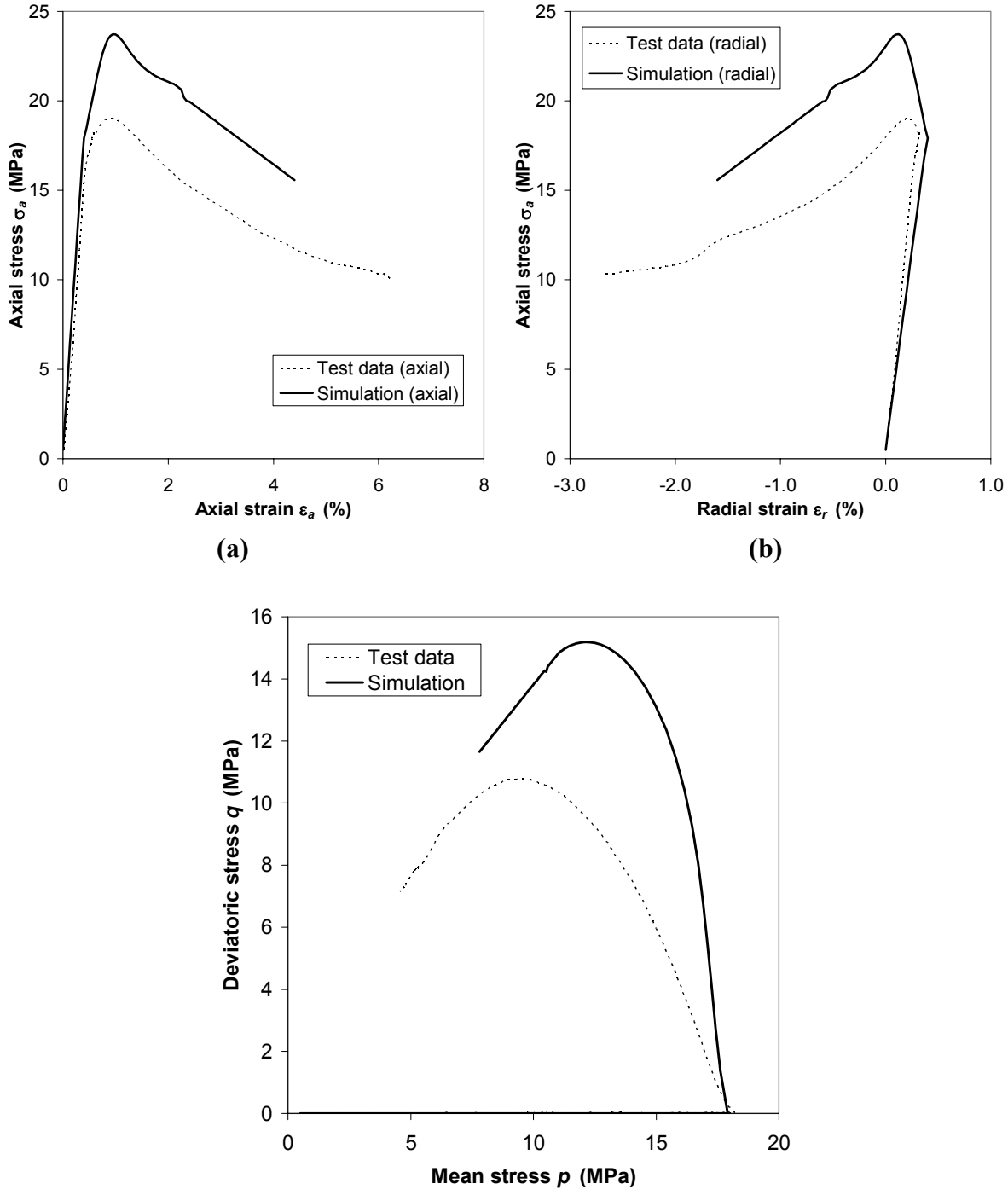

Figure 6.30. Experimental and simulated (a) axial and (b) radial stress-strain curves, and (c) stress paths for Valhall (Tor Fm.) chalk during undrained triaxial compression (File 434).

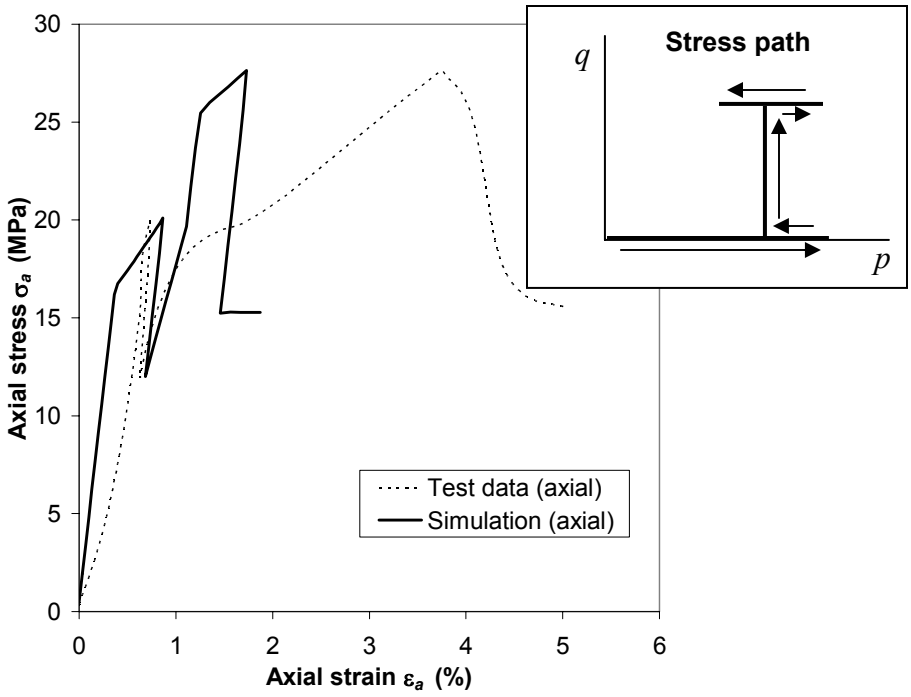

(a)

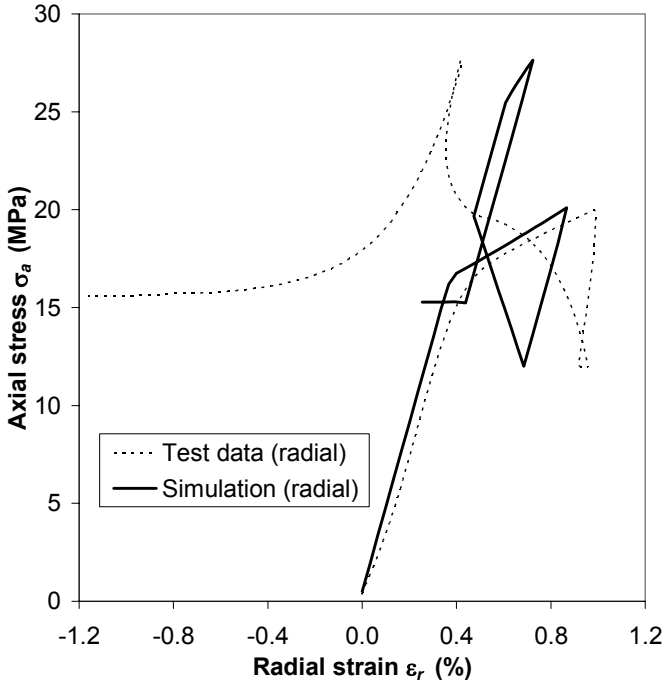

(b)

Figure 6.31. Experimental and simulated (a) axial and (b) radial stress-strain curves for Valhall (Tor Fm.) chalk under Stress Path 5 loading (File 327). Stress path shown in inset.

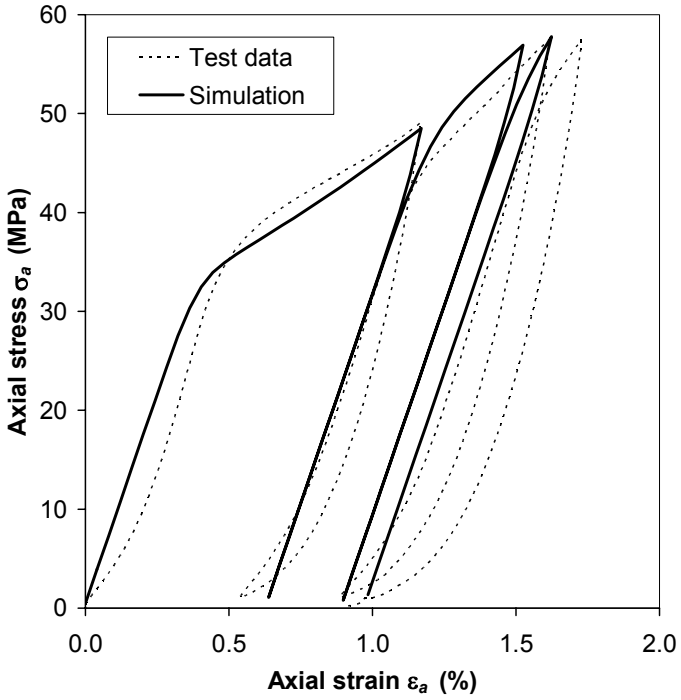

Figure 6.32. Experimental and simulated stress-strain curves for Dan chalk under cycled hydrostatic compression (File 310).

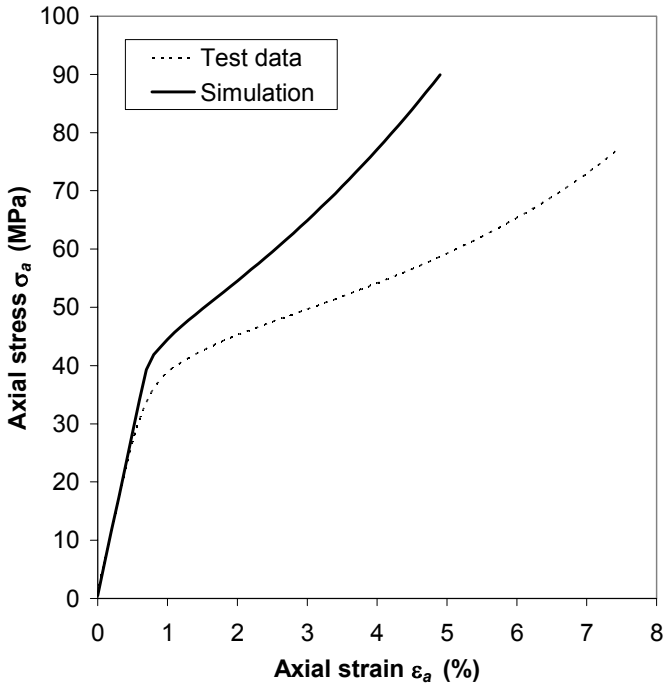

(a)

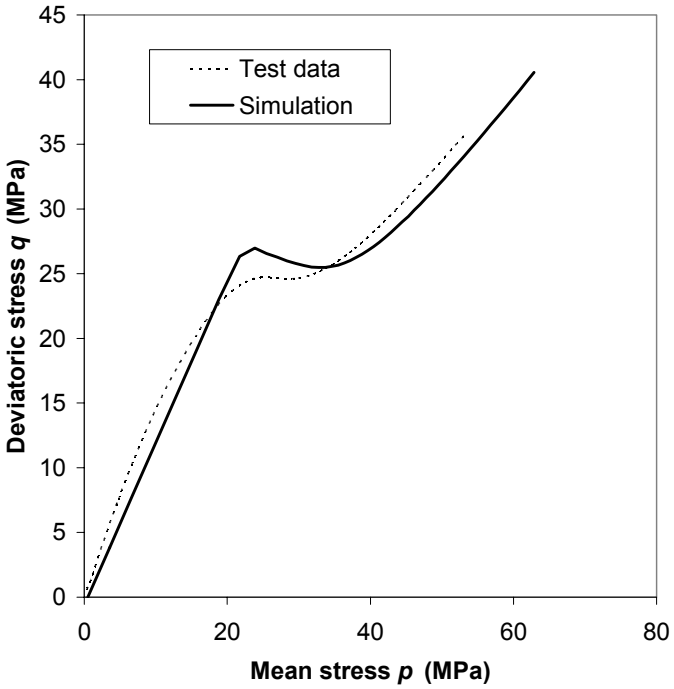

(b)

Figure 6.33. Experimental and simulated (a) stress-strain curves and (b) stress paths for Dan chalk under K_0 compression (File 311).

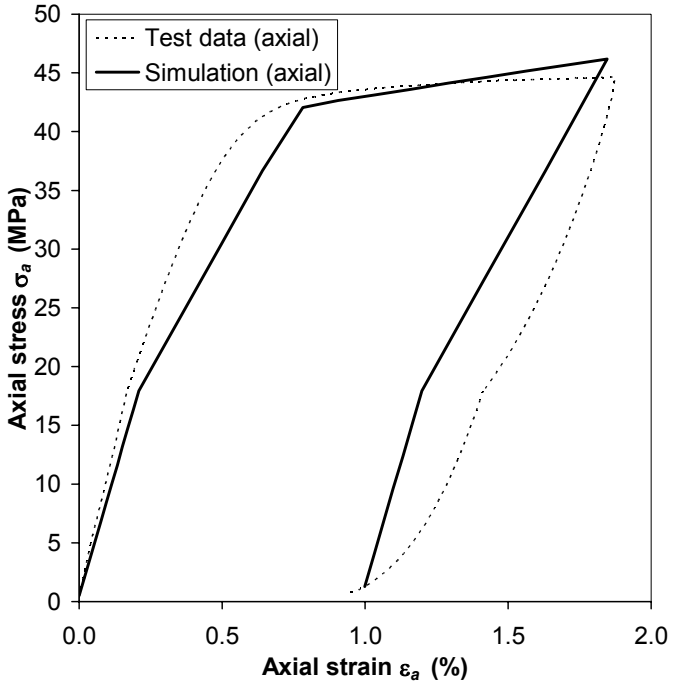

(a)

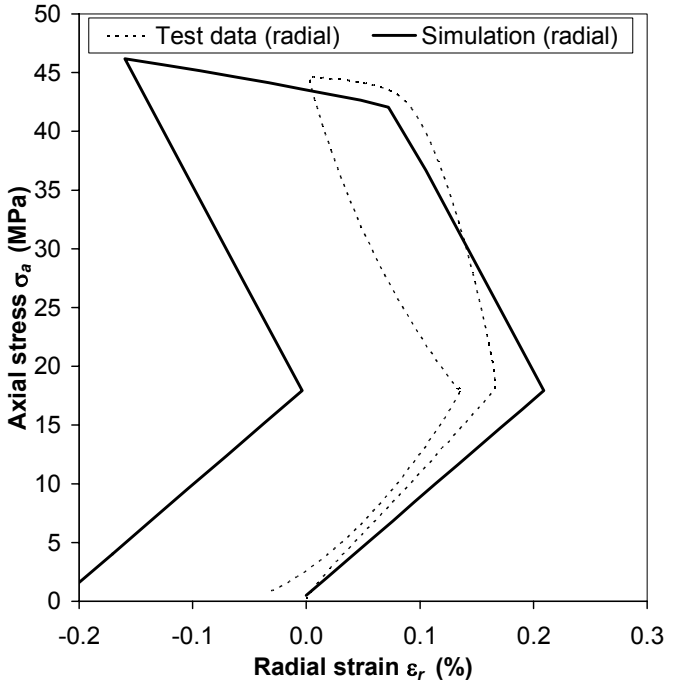

(b)

Figure 6.34. Experimental and simulated (a) axial and (b) radial stress-strain curves for Dan chalk under drained triaxial compression (File 312).

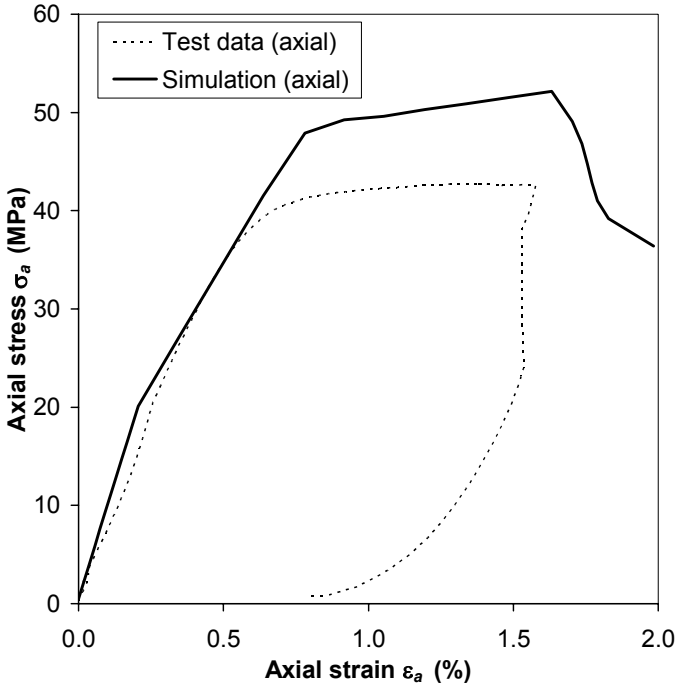

(a)

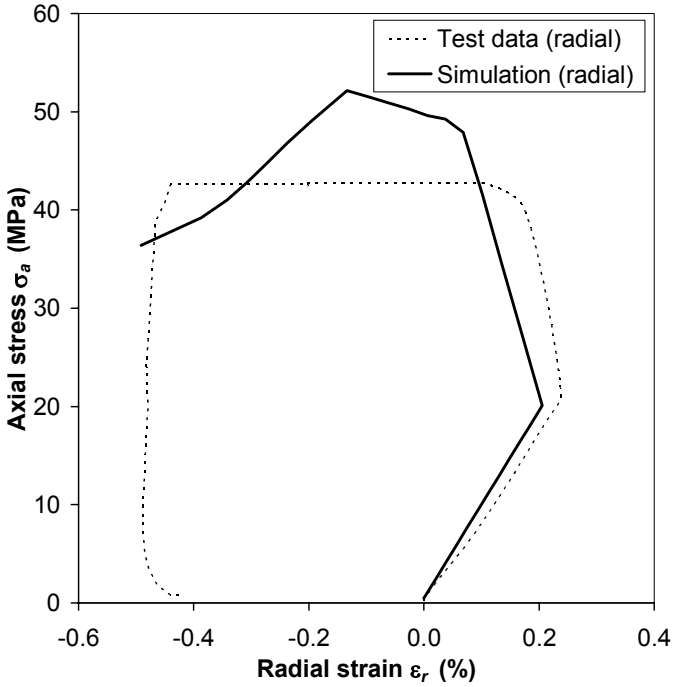

(b)

Figure 6.35. Experimental and simulated (a) axial and (b) radial stress-strain curves for Dan chalk under drained triaxial compression (File 315).

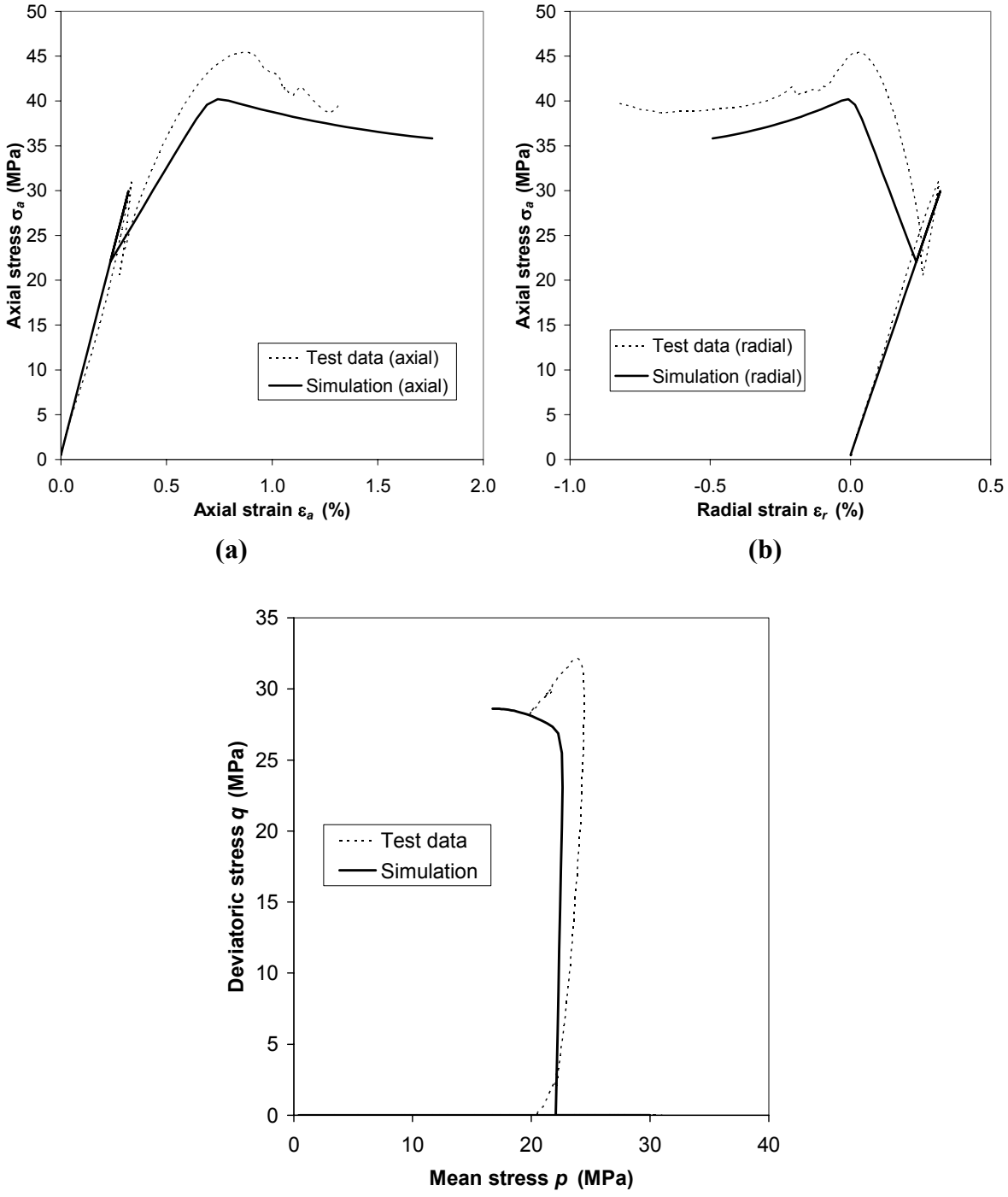

Figure 6.36. Experimental and simulated (a) axial and (b) radial stress-strain curves, and (c) stress paths for Dan chalk during overconsolided, undrained triaxial compression (File 316).

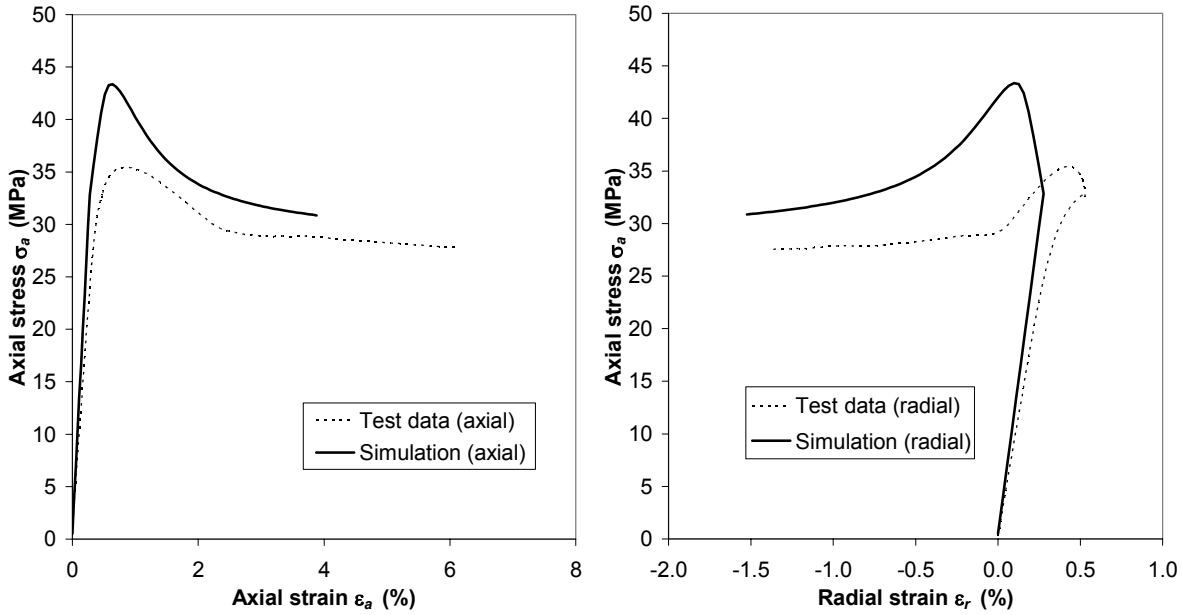

(a)

(b)

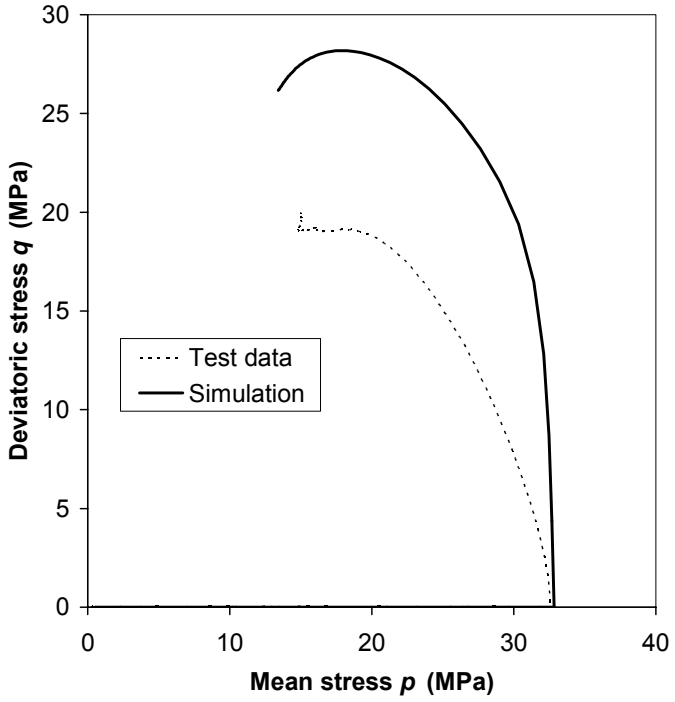

(c)

Figure 6.37. Experimental and simulated (a) axial and (b) radial stress-strain curves, and (c) stress paths for Dan chalk during undrained triaxial compression (File 420).

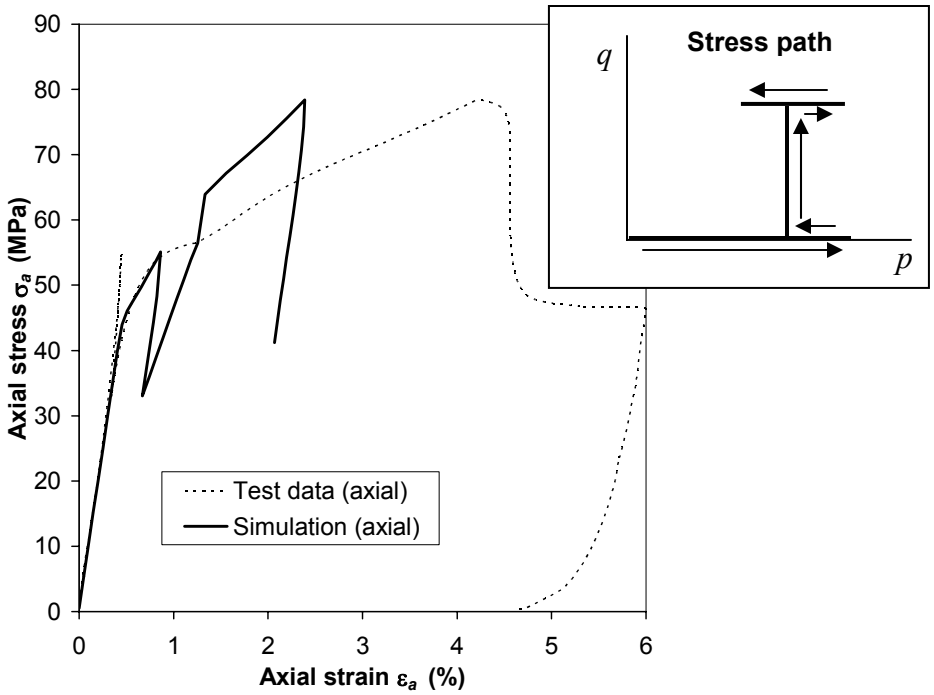

Figure 6.38. Experimental and simulated axial stress-strain curves for Dan chalk under Stress Path 5 loading (File 313). Stress path shown in inset.